Article

Retrograde movements determine effective stem cell numbers in the intestine

https://doi.org/10.1038/s41586-022-04962-0

Received: 18 February 2020

Accepted: 10 June 2022

Published online: 13 July 2022

Check for updates

Maria Azkanaz[1,2,19], Bernat Corominas-Murtra[3,4,19], Saskia I. J. Ellenbroek[1,2,19], Lotte Bruens[1,2,19], Anna T. Webb[5,19], Dimitrios Laskaris[1,2], Koen C. Oost[6], Simona J. A. Lafirenze[1,2,17], Karl Annusver[5], Hendrik A. Messal[1,2], Sharif Iqbal[7,8], Dustin J. Flanagan[9,18], David J. Huels[2,9,10], Felipe Rojas-Rodríguez[1], Miguel Vizoso[1,2], Maria Kasper[5], Owen J. Sansom[9,11], Hugo J. Snippert[2,12], Prisca Liberali[6,13], Benjamin D. Simons[14,15,16]✉, Pekka Katajisto[5,7,8]✉, Edouard Hannezo[4]✉ & Jacco van Rheenen[1,2]✉

The morphology and functionality of the epithelial lining differ along the intestinal tract, but tissue renewal at all sites is driven by stem cells at the base of crypts[1–3]. Whether stem cell numbers and behaviour vary at different sites is unknown. Here we show using intravital microscopy that, despite similarities in the number and distribution of proliferative cells with an *Lgr5* signature in mice, small intestinal crypts contain twice as many effective stem cells as large intestinal crypts. We find that, although passively displaced by a conveyor-belt-like upward movement, small intestinal cells positioned away from the crypt base can function as long-term effective stem cells owing to Wnt-dependent retrograde cellular movement. By contrast, the near absence of retrograde movement in the large intestine restricts cell repositioning, leading to a reduction in effective stem cell number. Moreover, after suppression of the retrograde movement in the small intestine, the number of effective stem cells is reduced, and the rate of monoclonal conversion of crypts is accelerated. Together, these results show that the number of effective stem cells is determined by active retrograde movement, revealing a new channel of stem cell regulation that can be experimentally and pharmacologically manipulated.

The intestinal tract consists of multiple compartments with different functions, together ensuring digestion and uptake of nutrients, absorption of water and expulsion of remainders of food intake. The small intestine (SI) comprises villi that project into the gut lumen and crypts that invaginate into the mucosa. The large intestine (LI), comprising the caecum and colon, has a similar crypt architecture to the SI, but lacks luminal-projecting villi. In both regions, mitotic stem cell zones form at the bottom of crypts, with more differentiated epithelial cells positioned towards the gut lumen. The entire intestinal tube is lined with a single layer of epithelial cells that gets renewed every few days. This high turnover has been shown to be the consequence of dividing stem cells that compete neutrally for niche space at the base of each crypt[1,2]. After each stem cell division, one cell becomes displaced upwards along the crypt–lumen axis to differentiate into specialized cells such as goblet cells and enterocytes. Markers, including leucine-rich repeat-containing G-protein-coupled receptor 5 (LGR5), have been associated with stem cell activity[3]. However, such markers do not necessarily label all or exclusively cells that have the potential to form clones that persist over the long term[4–8], which is considered here to be the defining property of effective stem cells. Using short-term intravital microscopy (IVM), we have previously shown that not every LGR5$^+$ cell has the same survival potential and therefore the potential to act as a long-term effective stem cell[9]. Compared with LGR5$^+$ cells positioned at the base of crypts, LGR5$^+$ cells further away are more susceptible to passive displacement and subsequent loss and therefore have a lower chance to form clones over the long term[9]. However, the distance from the crypt base at which cells have a realistic chance to function as long-term stem cells—that is, the number of effective stem cells—is currently unknown owing to technical constraints in intravital microscopy that prohibit following of the same clone over several weeks. Moreover, it is unknown whether stem cells behave similarly in the SI and LI, as intravital microscopy has mainly been focused on the

[1]Department of Molecular Pathology, The Netherlands Cancer Institute, Amsterdam, The Netherlands. [2]Oncode Institute, Utrecht, The Netherlands. [3]Institute of Biology, University of Graz, Graz, Austria. [4]Institute for Science and Technology Austria, Klosterneuburg, Austria. [5]Department of Cell and Molecular Biology (CMB), Karolinska Institutet, Stockholm, Sweden. [6]Friedrich Miescher Institute for Biomedical Research (FMI), Basel, Switzerland. [7]Institute of Biotechnology, HiLIFE, University of Helsinki, Helsinki, Finland. [8]Molecular and Integrative Bioscience Research Programme, Faculty of Biological and Environmental Sciences, University of Helsinki, Helsinki, Finland. [9]CRUK Beatson Institute, Glasgow, UK. [10]Laboratory for Experimental Oncology and Radiobiology, Center for Experimental and Molecular Medicine, Cancer Center Amsterdam, Amsterdam Gastroenterology Endocrinology and Metabolism, Amsterdam University Medical Centers, Amsterdam, The Netherlands. [11]Institute of Cancer Sciences, University of Glasgow, Glasgow, UK. [12]Molecular Cancer Research, Centre for Molecular Medicine, University Medical Centre Utrecht, Utrecht, The Netherlands. [13]University of Basel, Basel, Switzerland. [14]Wellcome Trust–Cancer Research UK Gurdon Institute, University of Cambridge, Cambridge, UK. [15]Department of Applied Mathematics and Theoretical Physics, Centre for Mathematical Sciences, University of Cambridge, Cambridge, UK. [16]Wellcome Trust–Medical Research Council Cambridge Stem Cell Institute, Jeffrey Cheah Biomedical Centre, University of Cambridge, Cambridge, UK. [17]Present address: Hubrecht Institute, Royal Academy of Arts and Sciences, University Medical Centre Utrecht, Utrecht, The Netherlands. [18]Present address: Biomedicine Discovery Institute, Monash University, Melbourne, Victoria, Australia. [19]These authors contributed equally: Maria Azkanaz, Bernat Corominas-Murtra, Saskia I. J. Ellenbroek, Lotte Bruens, Anna T. Webb. ✉e-mail: bds10@cam.ac.uk; pekka.katajisto@ki.se; edouard.hannezo@ist.ac.at; j.v.rheenen@nki.nl

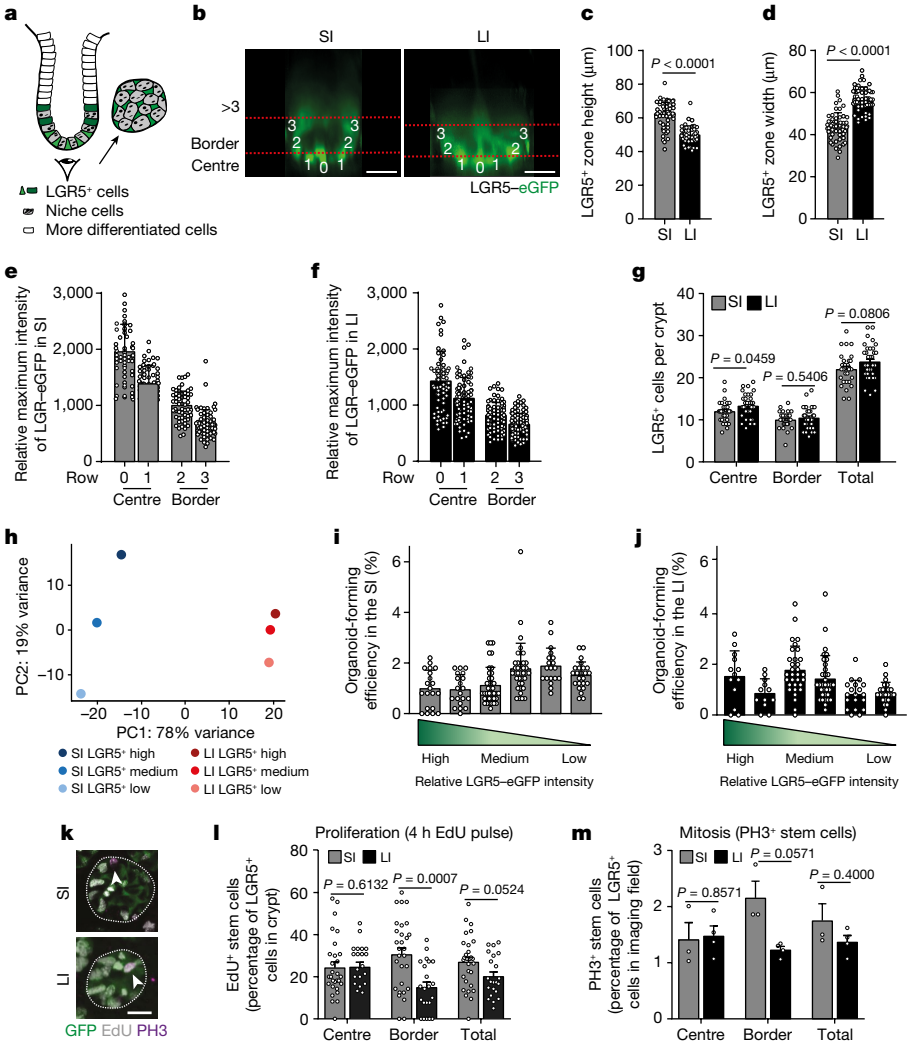

Fig. 1 | The spatial organization and functional potential of LGR5⁺ cells are comparable in the SI and LI. a, Schematic of the crypt. **b**, Representative *xy* images of SI and LI crypts in Lgr5eGFP-Ires-creERT2 mice from $n = 4$ experiments, showing the relative positions of LGR5⁺ cells in the central (rows 0 and 1) and border regions (rows 2 and 3) of the stem cell niche. **c**,**d**, The height (**c**) and width (**d**) of the LGR5–GFP⁺ zone in SI and LI. For **c** and **d**, $n = 50$ (SI) and $n = 48$ (LI) crypts. **e**, **f**, The relative maximum intensity of LGR5–eGFP signal in the SI (**e**) and LI (**f**). $n = 47$, $n = 62$, $n = 61$ and $n = 62$ (**e**); and $n = 66$, $n = 78$, $n = 77$ and $n = 84$ (**f**) crypts for rows 0, 1, 2 and 3, respectively. **g**, The number of LGR5⁺ cells in the centre and border and the total number in SI and LI crypts. $n = 50$ (SI) and $n = 48$ (LI) crypts. **h**, Principal component analysis of RNA-seq data of LGR5^{high}, LGR5^{medium} and LGR5^{low} cells (that is, centre, border and row >3 cells). **i**,**j**, The organoid-forming efficiency of LGR5⁺ cells with high, medium and low intensity isolated from the SI (**i**) and LI (**j**). The dots show the percentage of cells that formed organoids in a BME drop. From left to right, $n = 20$, $n = 20$, $n = 39$, $n = 38$, $n = 19$ and $n = 24$ (**i**); and $n = 13$, $n = 12$, $n = 32$, $n = 34$, $n = 19$ and $n = 24$ (**j**) BME drops from $n = 3$ experiments in $n = 3$ mice. **k**, Confocal images of LGR5–eGFP cells in S phase (4 h EdU) and mitosis (phosphorylated histone H3 (PH3), arrow heads) in SI and LI crypts (dotted outline). **l**,**m**, EdU⁺ (**l**) and PH3⁺ (**m**) LGR5⁺ cells as a percentage of the total LGR5⁺ pool in the SI ($n = 33$ crypts (**l**); $n = 3$ image fields (**m**)) and LI ($n = 22$ crypts (**l**); $n = 3$ image fields (**m**)). Data are mean ± s.e.m. For **c**, **d**, **l** and **m**, significance was determined using two-sided Mann–Whitney *U*-tests. For **b** and **k**, scale bars, 20 μm.

SI. Here we used intravital microscopy techniques that facilitate the monitoring of clones over multiple weeks in the SI and LI. By combining this analysis with 2D biophysical modelling of stem cell dynamics, we find that the numbers of effective stem cells in crypts differ between the SI and LI and that this is determined by the degree of Wnt-driven retrograde cell movement.

Characteristics of SI and LI crypts

To determine which cells act as effective stem cells in the SI and LI, we first looked at the total pool of LGR5⁺ cells at the crypt bases of Lgr5eGFP-Ires-creERT2 mice at both sites (Fig. 1a,b). The height of the LGR5⁺ zone is smaller in the LI than the SI, whereas the diameter of the crypt in the LI is larger than the SI (Fig. 1c,d). In both SI and LI crypts, LGR5⁺ cells are distributed over around four rows, with about five cells per row (Fig. 1b and Extended Data Fig. 1a). In both the SI and LI crypts, LGR5 expression is the highest for cells positioned at rows 0 and 1, and intermediate for cells positioned at rows 2 and 3, defined as centre and border LGR5⁺ cells, respectively (Fig. 1e,f). Cells positioned beyond row 3 express low levels of LGR5 (Fig. 1b). In both SI and LI crypts, the centre and border regions contain comparable numbers of LGR5⁺ cells (Fig. 1g), with a total of approximately 22–24 LGR5⁺ cells per crypt (Fig. 1g).

To test for potential differences in transcriptional level or colony-forming ability, we isolated LGR5⁺ cells from the centre, border and the region beyond the border (row >3) from both SI and LI crypts on the basis of their LGR5 expression using flow cytometry (Extended Data Fig. 1b). As expected, we observed differences in the transcriptional profile between centre and border LGR5⁺ cells within SI and LI crypts and more profound differences between the two intestinal sites (Fig. 1h and Extended Data Fig. 1c,d). Similar results were found when we

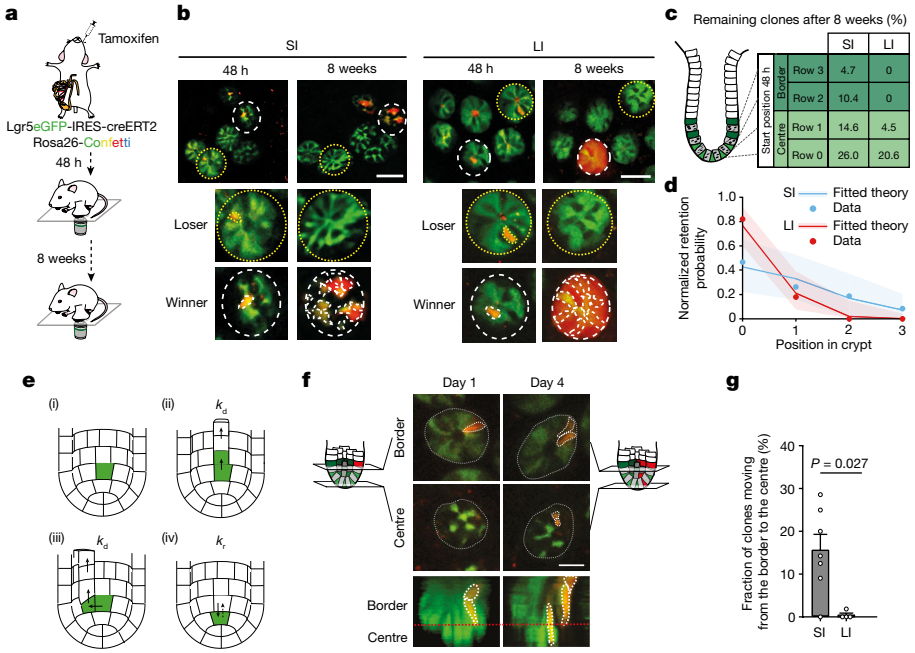

Fig. 2 | Different numbers of effective stem cells in the SI and LI due to retrograde movement. a, Schematic of the experimental set-up. **b**, Representative overview images 48 h and 8 weeks after tracing in the SI (left) and LI (right) from 6 independent experiments. The dotted yellow and white circles represent retraced crypts. A labelled clone can either be lost (loser, dashed yellow circle) or retained (winner, dashed white circle). **c**, Clone retention from different starting positions in the SI ($n = 267$ clones in $n = 6$ mice) and LI ($n = 294$ clones in $n = 6$ mice). **d**, Normalized retention probability at 8 weeks as predicted by the model (lines with 95% CI) and experimental data (dots) in the SI ($n = 267$ clones in $n = 6$ mice) and LI ($n = 294$ clones in $n = 6$ mice). **e**, Model sketch: the crypt is abstracted as a cylinder coupled to a hemispheric region (i). k_d is the upward movement rate due to cell division (ii and iii) and k_r is the random cell relocation rate, including retrograde movements (iv). **f**, Example of a border-starting clone at day 1 that moved to the centre at day 4 (retrograde movement) from 7 independent experiments. **g**, The percentage of border-starting clones present at the centre (retrograde movement) on day 3 in the SI ($n = 59$ clones in $n = 7$ mice) and LI ($n = 109$ clones in $n = 4$ mice). Data are mean ± s.e.m. Significance was determined using two-sided Mann–Whitney *U*-tests. Scale bars, 50 µm (**b**), 20 µm (**f**).

performed staining for other (stem cell) markers and Wnt targets (*Ascl2*, *Smoc2*, *Axin2*, *Cd44*, *Cycd1*, *Efnb2* and *Efnb3*) (Extended Data Fig. 1e–g). Importantly, regardless of any molecular differences, centre and border LGR5$^+$ cells showed similar potential to form organoids in growth-factor rich medium (Fig. 1i,j). These data suggest that LGR5$^+$ cells, regardless of their position within the crypt, have the potential to regain the full clonogenic ability when exposed to factors from the stem cell niche.

In addition to the number of LGR5$^+$ cells and their intrinsic molecular and functional potential, the cell division rate and the position of proliferating cells are important for the dynamics of stem cell competition as, together, they determine the rate at which stem cells are replaced in the niche. We compared the presence of proliferating cells in the SI and LI crypts by quantifying the number of cells in S phase (measuring short-term 5-ethynyl-2-deoxyuridine (EdU) incorporation) and the number of mitotic cells (positive for phosphorylated histone H3) (Fig. 1k–m). Our analyses revealed similar numbers of proliferating cells in the central crypt regions of the SI and LI (Fig. 1l,m). Moreover, we found that more cells in the border region of SI crypts were proliferating compared with those in the LI (Fig. 1l,m), resulting in a slightly higher fraction of proliferative cells in the SI overall. Notably, the proliferative zone above the LGR5$^+$ zone, known in the SI as the transit-amplifying zone, was significantly less pronounced in the colonic epithelium compared with the SI when assessed by BrdU incorporation (Extended Data Fig. 1h). Together, these results indicate that the spatial organization of LGR5$^+$ cells within crypts and their functional potential are overall comparable between the different intestinal compartments.

Effective stem cell numbers in the SI and LI

As the crypt architecture, including the distribution of cells with the same potential to regain the full clonogenic ability, was found to be similar, we next tested whether SI and LI crypts also contained similar numbers of effective stem cells. For this, we used our repetitive intravital microscopy techniques that enabled us to trace the progenies of LGR5$^+$ cells at different positions within the crypt over several weeks. The vasculature in large overview images was used as a landmark to find the same region, while images with higher resolution and magnification of the patchy expression of GFP and sporadic distribution of confetti-coloured crypts were used to validate the successful tracing of regions of interest (Extended Data Fig. 2a,b). This approach enabled us to retrace the same crypts over multiple imaging sessions and enabled us to study the fate of individual LGR5$^+$ cells over periods of months (Fig. 2a,b).

Using the multiday imaging approach, we recorded the locations of clones in crypt bases 48 h after induction and traced their fate 8 weeks later in Lgr5eGFP-Ires-creERT2;R26R-Confetti mice (Fig. 2a,b). Cells that gave rise to clones that persisted over the long-term were designated as effective stem cells (Fig. 2b (winner)). Quantification of clone retention (that is, the percentage of clones that remained present in the LGR5$^+$ zone) revealed that centre-derived clones were more likely to persist than border-derived clones, as expected on the basis of previous studies[9]. Notably, in the LI, no border-derived clones remained in the stem cell niche 8 weeks after the onset of tracing, whereas, in the SI, around 15% of border-derived clones continued to persist (Fig. 2c). Further dissection of different starting positions within the crypt bases revealed a gradient of positional advantage and clone retention probability, decreasing from centre to border (Fig. 2c,d), which was substantially steeper in the LI compared with the SI (Fig. 2d). These results indicate that, in contrast to the SI, LGR5$^+$ cells in the border of LI crypts do not function as effective stem cells. Together, we conclude that, during homeostasis, SI crypts contain more effective stem cells than LI crypts.

Modelling suggests retrograde movements

To better understand why LI border LGR5$^+$ cells do not function as effective stem cells while they have the intrinsic molecular and functional potential to do so, we turned to quantitative modelling. Previous studies have sought to model the neutral drift dynamics of clones around the crypt circumference using a minimal one-dimensional scheme[1] in which the effective stem cell number was linked to LGR5$^+$ expression[2] or fit using a continuous labelling strategy[10]. However, to understand how this effective stem cell number arises in the first place[11], we explicitly modelled the two-dimensional organization and biophysical cellular dynamics of the intestinal crypt (Supplementary Notes 1.1 and 2.1). In particular, we modelled individual crypts as regular two-dimensional cylindrical grids (denoting rows 0, 1 and so on as the cell position along the crypt–villus axis, with 5 cells per row, as measured in Extended Data Fig. 1a). In this model, cells undergo two core processes (sketched in Fig. 2e): (1) cell division at rate k_d (with random division orientation), leading to the upward transfer of cells along the crypt–villus axis (that is, anterograde movement); and (2) random cell relocation at constant rate k_r, leading to the exchange of neighbouring cells either within or between adjacent rows, allowing for additional directed onward or retrograde movement towards the crypt base. In the absence of retrograde movement (termed the deterministic conveyor belt model), cells at row 0 would systematically 'win' the competition over cells at rows >0, whereas non-zero values of k_r (the stochastic conveyor belt model) allow for cells at higher rows to participate in the competition, and function as effective stem cells. Crucially, this model makes the generic prediction that the probability of long-term clone retention should decrease with the distance from the bottom of the crypt as a Gaussian-like distribution, specifying a well-defined effective stem cell number that depends on only the dimensionless ratio k_r/k_d (that is, the ratio of relocation and division rates; Supplementary Note 1.2). Thus, this modelling suggests that differences in retrograde movement (that is, k_r) could provide a mechanistic explanation of the differential fate of the border LGR5$^+$ cells in the SI and LI.

Imaging retrograde movement intravitally

To test whether the difference in the ability of border LGR5$^+$ cells to function as effective stem cells is caused by differential retrograde movement in SI and LI crypts, we performed short-term multiday intravital microscopy in living Lgr5eGFP-Ires-creERT2;R26R-Confetti or Lgr5eGFP-Ires-creERT2;R26-LSL-tdTomato mice. Injection of a low dose of tamoxifen resulted in Cre-mediated recombination and activation of one of the Confetti colours or tdTomato, respectively, in individual LGR5-expressing cells. Using intravital microscopy on consecutive days, we monitored cell movement and clonal evolution of cells originally located at central or border regions over time in both the SI and LI (Fig. 2f). Positions and clone persistence were determined and quantified (Fig. 2f and Extended Data Figs. 2c,d and 3–6). As expected qualitatively from the model, retrograde movement of labelled cells was observed in the crypts of the SI, but was nearly absent in LI crypts (Fig. 2g). Consistent with the difference in retrograde movement, we confirmed the modelling predictions that clones that started from positions away from the crypt base (at levels 2 and 3) in LI crypts are lost faster than their counterparts in SI crypts (Fig. 2c,d and Extended Data Fig. 2c,d).

Wnt stimulates migration of LGR5$^+$ cells

Next, we aimed to determine the factors that drive retrograde cell movement. Recently, Wnt signalling has been shown to induce migration of intestinal stem cells in *Drosophila*[12]. Wnt has been implicated as one of the major niche factors to induce stem cell potential, and is produced by Paneth cells (PCs) and pericryptal stromal cells in SI crypts[13]. By contrast, LI crypts do not contain PCs[13]. To test whether PC-produced Wnt has the potential to induce migration of LGR5$^+$ cells, we isolated LGR5$^+$ cells by flow cytometry. Next, we seeded these cells onto ultra-low-attachment round-bottom plates and imaged their migration using confocal microscopy as previously described[14] (Supplementary Video 1). Interestingly, we observed that the mean square displacement of migratory cells was enhanced when cells were exposed to PCs (Fig. 3a,b), an effect caused by both enhanced speed and directional persistence (Extended Data Fig. 7). Importantly, this migration enhancement was abolished when the secretion of Wnt was inhibited by a porcupine inhibitor (IWP2) (Fig. 3a,b). These results suggest that PC-secreted Wnt can promote the migration of LGR5$^+$ cells. Indeed, when we directly stimulated LGR5$^+$ cells with exogenous Wnt, migration was enhanced even further (Fig. 3a,b and Extended Data Fig. 7).

To further validate the induction of retrograde movement by Wnt signalling, we decellularized the intestines from control and porcupine-inhibitor-treated mice (Fig. 3c). Such decellularized extracellular matrix scaffolds retain the original intestinal tissue architecture and multiple ECM bound factors that can provide positional cues guiding cell movement in vivo[15] (Fig. 3c). Next, we seeded single LGR5$^+$ cells on top of these scaffolds and observed using live microscopy that individual cells displayed highest motility along the z axis in crypts, an effect that was absent in villi (Fig. 3d and Supplementary Video 2). Moreover, cell motility along the z axis was decreased specifically in the crypts of those scaffolds that were prepared from mice treated with the porcupine inhibitor LGK974 (Fig. 3d).

Finally, we tested whether inhibition of Wnt release also blocks the retrograde movement that we observe in vivo. Previously, we have shown that reduced Wnt secretion after treatment with a low dose of LGK974 results in a lower number of effective stem cells[16]. By reanalysing[16] our intravital microscopy data, we indeed found that this change was correlated with a near abolition of retrograde cell movement (Fig. 3e) as well as decreased clone retention (Fig. 3f), whereas the cell proliferation rate was affected minimally by LGK974 treatment (Extended Data Fig. 8a,b). When combined, in addition to its classical role as a promoter of self-renewal in the base of crypts, our data suggest that Wnt stimulates cell migration and mediates retrograde cell movement.

Retrograde movement affects stemness

Our modelling and experiments suggest that Wnt-dependent retrograde movements enable border LGR5$^+$ cells to function as stem cells (that is, to function as an effective stem cell). However, the extent of this effect and the long-term consequence of differences in retrograde movement (that is, k_r) on effective stem cell number in the SI and LI crypts remained to be investigated quantitatively. The predicted Gaussian dependency of the probability of clone persistence as a function of initial position along the crypt–villus axis enabled us to define the number of effective stem cells in crypts (Fig. 2d) as the number of cells of which the lineage has a significant probability to persist over the long term (set above 5% for a given row, comprising 2σ of the fluctuations, where $\sigma^2 \propto k_r/k_d$; Supplementary Note 1.2).

Consistent with this simple prediction, which did not depend on the decided implementation of retrograde movements in the model (Supplementary Note 1.4), the clonal persistence at 8 weeks after induction as a function of starting position was well fitted by a Gaussian function in both the SI and LI. From this fit (Fig. 2d and Supplementary Note 2.2), we obtained: $k_r/k_d = 0.25$ in the LI (95% confidence interval (CI) = 0.05–0.55) and $k_r/k_d = 2$ in the SI (95% CI = 0.5–4.5).

We next estimated the consequence of differential k_r on the number of effective stem cells, N_s, using the predicted relationship (Supplementary Note 1.3):

$$N_s \approx N_g\left(1 + 2\sqrt{\frac{k_r}{k_d}}\right)$$

where $N_g = 5$ is the number of cells per row (Extended Data Fig. 1a). This led to a figure of $N_s^{SI} \approx 19$ effective stem cells per crypt in the SI

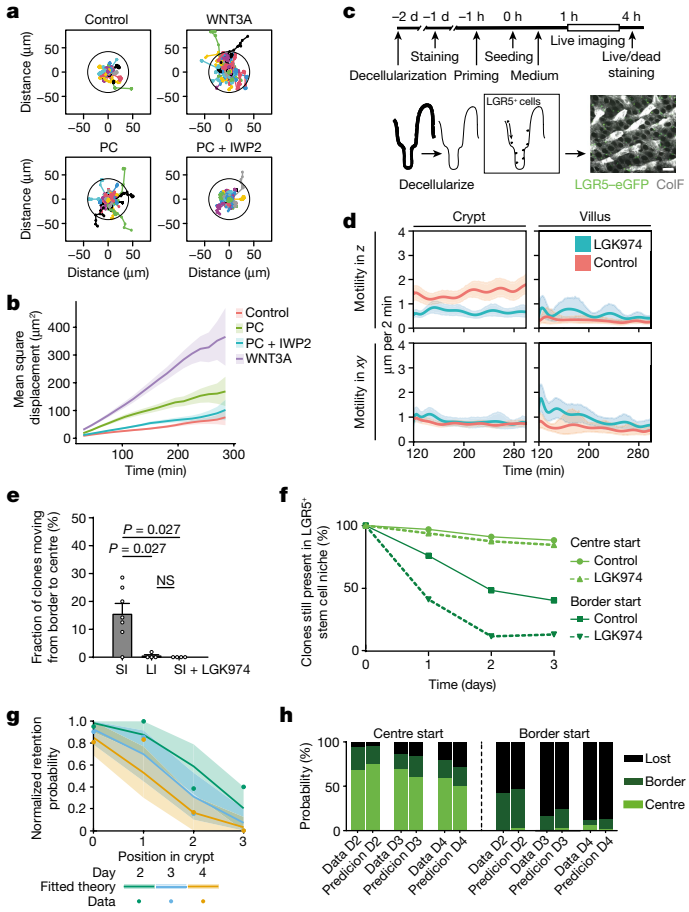

Fig. 3 | Wnt promotes LGR5⁺ cell migration. a, Normalized migration tracks of single LGR5⁺ cells isolated from LGR5-EGFP-ires-creERT2;R26R-confetti organoids in control medium; medium supplemented with WNT3A; co-culture with PCs; or co-culture PC with Wnt inhibitor (IWP2) in Matrigel. $n = 150$ random tracks of LGR5⁺ cells from $n = 2$ organoid lines, $n = 3$ biological replicates. **b**, Mean square displacement calculated as a function of time. $n = 150$ cells, $n = 3$ biological replicates. Data are mean ± s.e.m. **c**, Schematic of the experimental set-up for analysing cell movement on decellularized intestinal scaffolds. **d**, The motility of LGR5⁺ cells was determined along the crypt–villus axis (motility in the z axis) and along the lateral axis (motility in xy axes). $n = 150$–200 cell tracks from $n = 3$ decellularized intestines for each control- (vehicle) and LGK974-treated group. Data are mean ± 95% confidence interval. **e**, The percentage of border-starting clones present in the crypt centre (retrograde movement) on day 3. $n = 59$, $n = 109$ and $n = 75$ clones in $n = 7$, $n = 4$ and $n = 4$ mice for the SI and LI and the SI after LGK974 treatment, respectively. Data are mean ± s.e.m. Significance was determined using two-sided Mann–Whitney U-tests. **f**, Quantification of retention within the LGR5⁺ zone of centre- or border-starting clones in the crypts of control (solid lines) and LGK974-treated (dashed lines) mice as followed by IVM. $n = 75$ clones in $n = 4$ mice. **g**, The normalized retention probability in the LGR5⁺ zone in LGK974-treated SI ($n = 75$ clones in $n = 4$ mice; data reanalysed from ref. [16]) predicted by model (solid lines, mean ± 95% CI) and experimental data (dots). **h**, The probability of a clone starting either in the niche centre (left) or border (right) to be present in the centre, border or to be lost from the LGR5⁺ zone over time in the SI of LGK974-treated mice, comparing data (left bar) and theory (right bar). $n = 75$ clones in $n = 4$ mice (Supplementary Note 2.2.3). For **c**, scale bar, 50 μm.

(accounting for nearly all LGR5⁺ cells) and only around $N_s^{LI} \approx 10$ effective stem cells per crypt (translating to the first two rows) in the LI.

To validate experimentally the consequence of retrograde cell movement on the number of effective stem cells, we compared the evolution of clone retention as a function of starting position to predictions from numerical simulation and analytical theory, using the same values of k_r/k_d inferred above. For the short-term dynamics, the proliferation rate k_d also enters in the prediction, setting the overall time scale of the dynamics, with its inferred value broadly consistent with EdU data despite some variations between best-fit value between conditions, which could be related to short-term biases during lineage tracing (Supplementary Note 1 and Extended Data Fig. 9a–g). These results provided a good quantitative agreement at every time point for both the SI and LI (Extended Data Fig. 9h,i). Furthermore, the model and data showed an excellent quantitative agreement (the statistics are provided in Supplementary Note 2) for the retrograde movement of clones, indicating that differences in both short- and long-term dynamics in the SI and LI can be captured by our model (Extended Data Fig. 9j–m). Thus, the analysis of the short-term dynamics corroborates the findings of long-term lineage data and the values of k_r/k_d extracted above, confirming experimentally that the retrograde movement determines the effective stem cell number in the SI and LI crypts.

Next, we perturbed retrograde movement by inhibiting Wnt signalling using the porcupine inhibitor LGK974. Fitting the model to the dynamics of clone retention as a function of starting position confirmed that LGK974 treatment decreased k_r/k_d to 0.4 (95% CI = 0–1), resembling the value found in the LI during homeostasis. As well as providing a good fit of the clone retention dynamics (Fig. 3g), this ratio also predicted the rate of movement of clones between centre and border compartments (Fig. 3h and Supplementary Note 2.2).

Finally, we reasoned that a large retrograde movement rate k_r in the SI should also have a consequence for the spatial dispersion of clones along the crypt–villus axis. To test this, we performed short-term tracing, for which we reconstructed clones along the crypt–villus axis, both in the centre-border and beyond-border compartments. Importantly, we found that the probability of clone fragmentation was much higher in the SI than in the LI (Extended Data Fig. 10), and that the magnitude of the difference was well predicted by our 2D spatial model with the same parameters k_r/k_d extracted above, providing an independent confirmation for the predictions of the model. Together, these experiments further strengthen our conclusions that different short-term retrograde movement can explain differences in the long-term retention probability of crypt cells, and thereby dictate different effective stem cell numbers in SI and LI crypts.

Retrograde movement alters monoclonality

To examine the consequences of different effective stem cell numbers in SI and LI crypts, despite showing similar crypt characteristics and near-equal number of LGR5⁺ cells, we next compared the time that it takes for one clone to outcompete all others in a given crypt, that is, the time that it takes to reach crypt monoclonality. For this, we used whole-mount preparations of Lgr5eGFP-Ires-creERT2;R26R-Confetti mice that were euthanized at different time points after onset of lineage tracing (Fig. 4a). As predicted by our model, we observed differences in clonal expansion over time within the LGR5⁺ zone of SI and LI crypts, with faster evolution (that is, growth) of LI clones compared with SI clones (Fig. 4b). Monoclonality was reached faster in the LI than in the SI—whereas only around 30% of SI crypts were monoclonal at 6 weeks after onset of tracing, the vast majority of LI crypts was already monoclonal at that time (Fig. 4a,b). Notably, this evolution was predicted quantitatively by our model (Fig. 4c) with the different estimated ratios of k_r/k_d for each region (while the geometry—that is, the number of cells competing neutrally in a given row—and average cell division rate were equal). Moreover, our model prediction showed good agreement with the experimental long-term clonal evolution data after porcupine inhibitor treatment (Fig. 4d and Supplementary Note 2.4). Together, this argues that the process of monoclonal drift in intestinal crypts is faster in the LI than the SI, and can be enhanced by lowering the number of effective stem cells owing to reduced retrograde movement after porcupine inhibition.

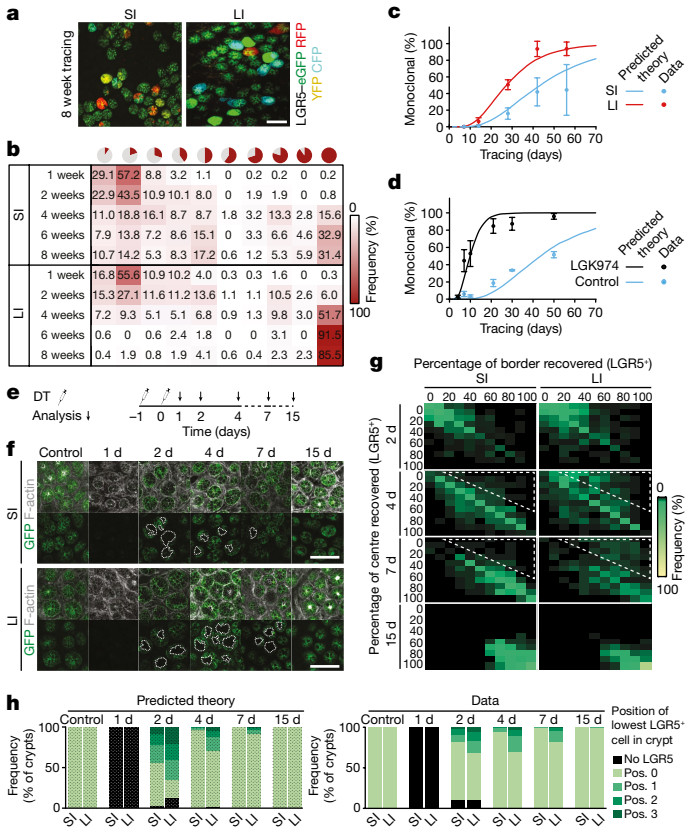

Fig. 4 | The consequences of retrograde movement. a, Representative maximum projections of crypt bottoms 8 weeks after induction in the SI and LI. $n = 5$ independent experiments. **b**, Heat map showing the frequency of clone sizes at different time points in the SI and LI. **c**, Monoclonal crypts in the SI and LI over time predicted by model (solid line) and real data in the SI and LI. Data are mean ± s.d. For **b** and **c**, $n = 444, 375, 218, 152$ and 151 clones in $n = 3, 4, 3, 5$ and 7 mice (SI); and $n = 304, 465, 236, 164$ and 531 clones in $n = 3, 4, 3, 5$ and 8 mice (LI) for 1, 2, 4, 6 and 8 weeks, respectively. **d**, Monoclonal crypts in the SI of control and LGK974-treated mice ($n = 3, 3, 4, 4, 3$ and 3 (control) and $n = 2, 4, 3, 5, 3$ and 3 (LGK974) mice for days 4, 7, 10, 21, 30 and 50, respectively; $n = 200$ clones per mouse) over time predicted by model (solid line) and real data reanalysed from ref. [16]. Data are mean ± s.e.m. (Supplementary Note 2.2.3). **e**, Schematic of DT treatment. Targeted ablation of LGR5$^+$ cells by two DT injections in 19 *Lgr5DTR:EGFP* mice. **f**, Representative images of untreated and DT-treated mice at different time points after ablation. $n = 3$ independent experiments. **g**, Heat map of the percentage of crypts recovered in the centre and border regions in the SI and LI. $n = 5, 3, 4$ and 3 mice for days 2, 4, 7 and 15, respectively. Note the faster recovery kinetics of SI crypts (white dashed triangles). **h**, The best numerical fit for the position of the lowest LGR5$^+$ cell using the biophysical model (left), predicting faster dynamics in the presence of a larger amount of retrograde movements, and experimental data (right). $n = 2, 3, 5, 3, 4$ and 3 mice for control, day 1, 2, 4, 7 and 15, respectively. Scale bars, 200 µm (**a**) and 100 µm (**f**).

Retrograde movement affects regeneration

Movement of cells from the transit-amplifying zone into the stem cell zone has been shown to be important for the regeneration of the stem cell pool following their loss[17]. Thus, to test whether distinct retrograde movement in SI and LI crypts also affects regeneration of the stem cell pool, we traced the recovery of the SI and LI LGR5$^+$ cell compartment after targeted ablation of LGR5$^+$ cells using diphtheria toxin (DT) injection in mice in which the human DT receptor (DTR) fused to eGFP was knocked into the *Lgr5* locus (*Lgr5DTR:eGFP*)[17]. We measured the recovery of LGR5–DTR–GFP cells at various cell positions in the crypt (Fig. 4e–g). We first performed this experiment in silico using our mathematical framework (Fig. 4h (left)). Owing to differences in the retrograde movement, our framework predicted that the recovery of the stem cell pool in the SI should be faster than in the LI, especially regarding the stem cells in the centre of the niche (position 0 and 1). Notably, we indeed observed such distinct behaviour in the experiment (Fig. 4h (right)). Although the recovery of centre LGR5$^+$ cells was nearly complete after 4 days in the SI, a large proportion of the LI crypts still lacked a centre LGR5$^+$ cell after 7 days (Fig. 4h (right) and 4g (white dotted area)). Combined, these data suggest that the retrograde movement supports fast regeneration of the LGR5$^+$ cell pool.

Discussion

Stem cells are defined by their potential to self-renew and give rise to differentiated progeny. Traditionally, stem cell potential has been thought to be an intrinsic property that is induced by cues such as Wnt, and characterized by signature expression of molecular markers such as *Lgr5*. Although LGR5$^+$ cells in intestinal crypts have the intrinsic ability to give rise to all differentiated cell types and to form in vitro organoid cultures, LGR5 expression does not necessarily overlap with the ensemble of cells showing functional stem cell activity[4–8]. Here we have shown that, in addition to the passive rearrangements of cells after proliferation (that is, cells that are displaced by others), Wnt-driven active retrograde movement (that is, cells that move by themselves in the opposite direction of anterograde movement) determines the number of effective stem cells in intestinal crypts. Although LGR5$^+$ cells at the border of the LI crypt base (rows 2 and 3) are exposed to the stem-cell-inducing niche and have all of the properties to function as stem cells, we find that, owing to lack of retrograde movement, these cells are not able to form long-term clones and act as effective stem cells as they get continuously displaced by the progeny of LGR5$^+$ cells located at lower rows. By contrast, owing to the presence of retrograde movement in SI crypts, cells at the border of the crypt base, possibly including those outside the LGR5$^+$ zone, can take turns to visit the crypt centre, and therefore have a chance to function as long-term effective stem cells. Thus, we conclude that stem cell identity is neither cell intrinsic nor marked by distinct molecular signatures but, rather, is defined by the potential of cells to be present in or enter a location that both induces self-renewal and prevents displacement.

Our experimental data and mathematical modelling demonstrate the importance of random cell relocation and retrograde movement in governing stem cell identity, and show surprising differences in the rate and dynamics of monoclonal conversion in the SI versus LI, despite strong similarities in crypt characteristics. Our model identifies a single dimensionless parameter, that is, the ratio between cell repositioning rate and division rate (k_r/k_d), which sets the spatial extent of the effective stem cell region, defined as the length along the axis of the crypt at which cells have a significant probability to contribute to long-term renewal. In the LI, k_r and, therefore, retrograde movement is so minimal that self-renewal potential is largely limited to cells positioned at row 0 (that is, approximately 5–10 stem cells compete laterally and neutrally), whereas more complex dynamics emerge in the SI due to retrograde movements, with neutral competition between cells of the same row[1,2] as well as biased competition between cells of different rows (stochastic conveyor belt).

Importantly, the differential rate of cell repositioning and retrograde movement was sufficient to explain the differential dynamics underlying regeneration of the stem cell pool, competition for niche space in the SI and LI, as well as the faster clonal evolution and shorter fixation times in the LI compared to the SI. This underlines the importance of a better understanding of the molecular and cellular bases of retrograde movements. Interestingly, we observed less retrograde movement after porcupine inhibition, whereas proliferation was unaltered. This was consistent with complementary experiments from in vitro and decellularized migration assays, indicating a role for Wnt signalling in driving active migratory movements even in regions beyond the crypt base with low levels of Wnt.

To induce self-renewal in the Wnt-rich region, the pericryptal stroma is a sufficient Wnt source in the absence of PCs[18,19]. However, for retrograde movement, this source is insufficient as this movement is not present in the LI. Seemingly, for movements in regions beyond the crypt base, other Wnt sources, such as PCs in the SI, are required. Although the low levels of Wnt outside the crypt base may be insufficient to induce self-renewal properties, our data suggest that these levels are high enough to induce migration enabling cells to enter Wnt-rich regions. As Wnt is known to regulate numerous other processes, including induction of self-renewal, it remains difficult to directly provide causality between stem cell function and retrograde movement. Nevertheless, our results suggest that retrograde movements in the SI are not only a result of random repositioning during cell division, but represent a new level of active stem cell regulation that can be experimentally and pharmacologically manipulated. In this regard, it is also interesting that Wnt-antagonists are increased during ageing[20] and early adenoma formation[21]. Given the importance of homeostatic stem cell dynamics in predicting the response of the cellular compartments to non-neutral mutations, the retrograde movement shown here may contribute to susceptibility to pathological conditions such as tumour initiation along the intestinal tract.

Online content

Any methods, additional references, Nature Research reporting summaries, source data, extended data, supplementary information, acknowledgements, peer review information; details of author contributions and competing interests; and statements of data and code availability are available at https://doi.org/10.1038/s41586-022-04962-0.

1. Lopez-Garcia, C., Klein, A. M., Simons, B. D. & Winton, D. J. Intestinal stem cell replacement follows a pattern of neutral drift. *Science* **330**, 822–825 (2010).
2. Snippert, H. J. et al. Intestinal crypt homeostasis results from neutral competition between symmetrically dividing Lgr5 stem cells. *Cell* **143**, 134–144 (2010).
3. Barker, N. et al. Identification of stem cells in small intestine and colon by marker gene Lgr5. *Nature* **449**, 1003–1007 (2007).
4. Breault, D. T. et al. Generation of mTert-GFP mice as a model to identify and study tissue progenitor cells. *Proc. Natl Acad. Sci. USA* **105**, 10420–10425 (2008).
5. Powell, A. E. et al. The pan-ErbB negative regulator Lrig1 is an intestinal stem cell marker that functions as a tumor suppressor. *Cell* **149**, 146–158 (2012).
6. Sangiorgi, E. & Capecchi, M. R. Bmi1 is expressed in vivo in intestinal stem cells. *Nat. Genet.* **40**, 915–920 (2008).
7. Takeda, N. et al. Interconversion between intestinal stem cell populations in distinct niches. *Science* **334**, 1420–1424 (2011).
8. Barriga, F. M. et al. Mex3a marks a slowly dividing subpopulation of Lgr5^{+} intestinal stem cells. *Cell Stem Cell* **20**, 801–816 (2017).
9. Ritsma, L. et al. Intestinal crypt homeostasis revealed at single-stem-cell level by in vivo live imaging. *Nature* **507**, 362–365 (2014).
10. Kozar, S. et al. Continuous clonal labeling reveals small numbers of functional stem cells in intestinal crypts and adenomas. *Cell Stem Cell* **13**, 626–633 (2013).
11. Corominas-Murtra, B. et al. Stem cell lineage survival as a noisy competition for niche access. *Proc. Natl Acad. Sci. USA* **117**, 16969–16975 (2020).
12. Hu, D. J., Yun, J., Elstrott, J. & Jasper, H. Non-canonical Wnt signaling promotes directed migration of intestinal stem cells to sites of injury. *Nat. Commun.* **12**, 7150 (2021).
13. Gregorieff, A. et al. Expression pattern of Wnt signaling components in the adult intestine. *Gastroenterology* **129**, 626–638 (2005).
14. Sato, T. et al. Paneth cells constitute the niche for Lgr5 stem cells in intestinal crypts. *Nature* **469**, 415–418 (2011).
15. Iqbal, S. et al. Fetal-like reversion in the regenerating intestine is regulated by mesenchymal Asporin. Preprint at *bioRxiv* https://doi.org/10.1101/2021.06.24.449590 (2021).
16. Huels, D. J. et al. Wnt ligands influence tumour initiation by controlling the number of intestinal stem cells. *Nat. Commun.* **9**, 1132 (2018).
17. Tian, H. et al. A reserve stem cell population in small intestine renders Lgr5-positive cells dispensable. *Nature* **478**, 255–259 (2011).
18. Durand, A. et al. Functional intestinal stem cells after Paneth cell ablation induced by the loss of transcription factor Math1 (Atoh1). *Proc. Natl Acad. Sci. USA* **109**, 8965–8970 (2012).
19. Kim, T. H., Escudero, S. & Shivdasani, R. A. Intact function of Lgr5 receptor-expressing intestinal stem cells in the absence of Paneth cells. *Proc. Natl Acad. Sci. USA* **109**, 3932–3937 (2012).
20. Pentinmikko, N. et al. Notum produced by Paneth cells attenuates regeneration of aged intestinal epithelium. *Nature* **571**, 398–402 (2019).
21. Flanagan, D. J. et al. NOTUM from Apc-mutant cells biases clonal competition to initiate cancer. *Nature* **594**, 430–435 (2021).

Methods

Mice and treatment

All animal experiments were carried out in accordance under the guidelines and approval of the animal welfare committee of the Netherlands Cancer Institute and Hubrecht Institute (KNAW). The following mouse strains were used: Lgr5eGFP-Ires-creERT2[3]; R26-LSL-tdTomato[22] and R26-confetti[2]. For lineage tracing experiments, Lgr5eGFP-Ires-creERT 2;R26-Confetti and Lgr5eGFP-ires-creERT2;LSL-tdTomato mice were used. Lgr5eGFP-Ires-creERT2 were used to isolate LGR5$^+$ cells and C57/B6 mice were used to decellularize intestines for the decellularized intestine experiment. LGR5-DTR-GFP[17] mice were used for the LGR5$^+$ cell ablation experiments. Genentech provided the LGR5-DTR-GFP mice through their MTA program. Mice (mixed or C57/B6 background) were housed under standard laboratory conditions in SPF cages in an animal room at constant temperature (19–23 °C) and regulated humidity under a 12 h–12 h light–dark cycle and received standard laboratory chow and water ad libitum. Male and female mice between 8 and 50 weeks of age were used for static lineage tracing and IVM experiments. For whole-mount imaging and imaging of isolated crypts, RNA-seq, colony-forming assay, decellularized intestine, LGR5$^+$ cell ablation and clone dispersion experiments, intestines from 8–50 week-old male and female mice were used. Strains were bred in house. LGR5eGFP-Ires-creERT2;R26-Confetti received 1 mg tamoxifen (Sigma-Aldrich) for IVM lineage tracing experiments and 5 mg tamoxifen (Sigma-Aldrich) for static lineage-tracing experiments. For long-term (intravital) tracing, small and large intestines were taken from the same mouse. This was not possible for short-term intravital microscopy experiments, as only either the small or large intestine fitted behind the abdominal imaging window (AIW). For the decellularized intestine experiment, the porcupine inhibitor LGK974 was administered at a concentration of 5 mg kg^{-1} BID (oral) in a vehicle of 0.5% Tween-80/0.5% methylcellulose. Mice of the same litter were randomly assigned to each condition regardless of the sex. Different conditions were imaged and analysed in a random manner to minimize potential cofounding factors. No statistical methods were used to predetermine sample size estimates.

Surgery

All surgical procedures were performed under ~2% isoflurane (v/v) inhalation anaesthesia. Before and 8–12 h after surgery, mice were treated with a dose of buprenorphine (subcutaneous, 100 µg kg^{-1} mouse, Temgesic; BD Pharmaceutical System). Rimadyl (64 µg ml^{-1}, Carprofen; Zoetis) was given in drinking water for 3 days after the surgery. For short-term intravital microscopy, an AIW was placed as described previously[23]. In brief, the left lateral flank of the mouse was shaved and disinfected. An incision was made through the skin and peritoneum of the mouse and a purse string suture was placed along the edge of the wound. The ileum (SI) or caecum (LI) was exposed and a disinfected AIW (>1 h in 70% (v/v) ethanol) was placed on top. In the case of the ileum, the mesenterium was fixed to the cover glass using Cyanoacrylate Glue (Pattex) and CyGel (BioStatus) was added on top to prevent liquid accumulation. In the case of the caecum, it was fixed to the titanium ring of the AIW using Cyanoacrylate Glue (Pattex). When these substances were dry, the intestines and AIW were placed back into the abdominal cavity and the skin and abdominal wall were placed into the groove of the AIW. Subsequently, the suture was tightened. After surgery, the mice were closely monitored daily for reactivity, behaviour, appearance and defecation. For repetitive long-term imaging, parts of the intestine that were imaged were exteriorized through a midline abdominal incision. Tissue hydration was maintained by creating a wet chamber, covering the mice with parafilm and the exposed tissue with PBS-drenched gauze. After the imaging session imaged tissue was placed back in the abdomen and the abdomen was closed using vicryl absorbable sutures (GMED Healthcare).

Intravital microscopy

For every imaging session, mice were sedated using isoflurane inhalation anaesthesia (~1.5% isoflurane/O_2 mixture) and placed into a custom-designed imaging box. For short-term imaging, mice were imaged once a day for a maximum of 3 h. For long-term imaging, mice were imaged 2–3 days after label induction and 8 weeks thereafter. *z*-Stacks and overview images were recorded using the Navigator function from Leica. The patchy expression pattern of the *Lgr5* knockin allele, in combination with specific landmarks such as blood vessels, enabled repeated identification of imaged areas over consecutive days. After imaging, only if necessary, the acquired images were corrected for bleed through, cropped, smoothened, rotated and contrasted linearly in Fiji (v.2.3.0) (https://imagej.nih.gov/ij/).

Whole-mount preparation

For whole-mount imaging, intestines were collected and the lumen was flushed with ice-cold PBSO. The tissues were opened longitudinally and for the ileum, villi were removed from the luminal surface using a cover glass. The tissues were washed in ice-cold PBSO and fixed for 30 min in 4% formaldehyde solution (w/v) (Klinipath)) or periodate-lysine-4% paraformaldehyde (PLP) overnight at 4 °C (ref. [24]). For antibody labelling, the tissues were permeabilized in 0.8% Triton X-100 in PBS containing 3% BSA. Subsequently, stretches of ~2 cm of fixed tissue, were mounted between 2 coverslips and embedded in Vectashield HardSet Antifade Mounting Medium (Vector Laboratories). Crypts were imaged from the bottom using the same equipment and settings as for intravital microscopy described below. For storage, PLP-fixed tissues were incubated in sucrose for >6 h and frozen in OCT at −80 °C.

Crypt isolation

For crypt isolation, intestines were collected and the lumen was flushed with ice-cold PBS. Tissue was opened longitudinally, villi were removed from the luminal surface of distal ileum. Parts of approximately 3 cm of ileum and intact but opened caecum were incubated with 30 mM in EDTA in HBSS at room temperature for 20 min. After vigorously shaking, the release of the epithelium from the mesenchyme was checked using a microscope. Suspensions were filtered (100 µm) before centrifuging (5 min at 4 °C, 88 rcf). Pellets containing isolated crypts were washed with cold PBS, fixed in 4% PFA (30 min at room temperature), permeabilized in 1% Triton X-100 (45 min at room temperature), blocked in blocking buffer for 30 min at room temperature (1% BSA, 3% horse serum, 0.2% Triton X-100 in PBS) before antibody labelling.

Cell proliferation and antibody labelling

To label cells in S phase, 1 mg of EdU (200 µl in PBS) or 2 mg bromodeoxyuridine (BrdU, 200 µl in PBS) was injected intraperitoneally 2 h or 4 h before euthanasia (indicated in the figure legends). Tissues were processed for whole-mount analysis or crypt isolation as described above. The Click-it staining reaction was performed according to the manufacturer's protocol (Click-it EdU, Thermo Fisher Scientific/Invitrogen). For labelling of BrdU incorporation, crypts were incubated in 2 N HCl at 37 °C for 15 min to denature the DNA followed by 15 min in 0.1 M sodium borate for neutralization before incubation with anti-BrdU antibodies (1:50, Abcam, 6326) and anti-GFP antibodies (1:200, Abcam, 6673) overnight. To label cells during mitosis, anti-phosphorylated histone H3 antibodies were used (1:200, Millipore, 06-570). To visualize ephrin B2 and B3, intestines were stained with anti-ephrin-B2 antibodies (1:100, R&D Systems, AF467) and anti-ephrin-B3 antibodies (1:100 R&D Systems, AF432). Stainings were finalized by incubation with Alexa Fluor secondary antibodies, donkey anti-goat IgG Alexa Fluor 488 (A-11055), donkey anti-rabbit IgG (H+L) Alexa Fluor 568 (A-10042) and chicken anti-rabbit IgG (H+L) Alexa Fluor 647 (A-21443) (1:200 Invitrogen) combined with DAPI followed by mounting in antifading mounting medium (Vectashield, Vector laboratories). To visualize Wnt

target gene expression, formalin-fixed intestinal tissue was incubated with the following Primary antibodies as previously described[21]: CD44 (1:50 BD Biosciences, 550538), cyclin D1 (1:50, Dako, M3635).

RNA in situ hybridization

In situ hybridization for *Lgr5* (312178), *Smoc2* (318548), *Ascl2* (412218) and *Axin2* (400338) mRNA (all from Advanced Cell Diagnostics) was performed using RNAscope 2.5 LS Reagent Kit–BROWN (Advanced Cell Diagnostics) on a BOND RX autostainer (Leica) according to the manufacturer's instructions.

Microscopy equipment and settings

Tissues were imaged with an inverted Leica TCS SP8 confocal microscope. All images were collected in 12 bit with ×25 water immersion objective (HC FLUOTAR L N.A. 0.95 W VISIR 0.17 FWD 2.4 mm).

Sample preparation for RNA-seq and colony-formation assay

Small and large intestinal crypts were isolated as previously described[25]. To obtain single cells, crypts were treated with TrypLE (Life Technology) supplemented with 30 μg ml^{-1} DNase I (Sigma-Aldrich) and Y-27632 (10 μM) (incubation at 37 °C for 30 min). Dissociated cells were filtrated through a 100 μm cell strainer (Greiner Bio-One), and cells were resuspended and incubated with antibodies for 30 min on ice in 1 ml PBS containing FCS 5%, EDTA 5 mM (Accugene, Lonza), B27 2% (Thermo Fisher Scientific, 17504-044), *N*-acetylcysteine 1.25 mM (Sigma-Aldrich, A9165), mEGF 50 ng ml^{-1} (Peprotech, 315-09), noggin and R-spondin1 (both 10%; conditioned medium prepared in house), Y-27632 (1 μM) and 4 μg ml^{-1} DNase I (Sigma-Aldrich). The cell suspension was filtered through a 70 μm cell strainer (Celltrix) and analysed using flow cytometry on the FACS Aria Fusion (BD Biosciences) system. Dead cells were eliminated by gating of forward/side scatter, forward/pulse-width parameters and negative staining for 7-AAD (eBioScience). LGR5$^+$ cells were sorted by positive staining for Epcam (CD326) (BD Bioscience, 563214) and endogenous LGR5–GFP signal. Data were visualized using FlowJo v.10.6.1 (https://www.flowjo.com/).

For RNA-seq, sorted cells were collected into 1.5 ml tubes containing FACS buffer, washed with PBS, pelleted and stored at −80 °C for further processing. RNA was isolated using RNeasy Micro Kit (Qiagen).

For colony-formation assays, sorted cells were collected in FACS buffer, washed with PBS, pelleted and embedded in Cultrex PathClear Reduced Growth Factor Basement Membrane Extract Type 2 (BME2) (Amsbio, 3533-005-02), followed by seeding onto 24-well plate (500 cells in 20 μl of BME2 per well). The number of organoids were counted 7 days after seeding.

Processing RNA-seq expression data

For library preparation, the SMART-Seq Stranded Kit (Takara) was used. Sequencing was performed by CeGaT on the NovaSeq 6000 system with 100 bp paired-end reads. Demultiplexing of sequencing reads for all 18 samples (three biological replicates of LGR5$^+$ high, medium and low cells for both SI and LI) was performed using Illumina bcl2fastq (v.2.20) for which adapters were trimmed using Skewer (v.0.2.2)[26]. Trimmed raw reads (average length 96–102 nucleotides) were aligned to the mm10 genome using STAR (v.2.5.2b)[27] for genome assembly and gene count.

Differential expression analysis was performed between groups considering biological replicates of intestinal locations using DeSeq2 (v.1.34 in Bioconductor v.3.14)[28] in R (v.4.1.1; R Core Team 2021). After normalization, all regions with a mean count greater than zero were included to improve detection power. The mean count across genes above zero was selected based on the standard deviation for each genes. With normalized counts we calculated the $\log_2$-transformed fold change and obtained the *P* value (Wald test) and *P* value adjusted using Benjamin–Hochberg correction for multiple testing.

The relationships between intestinal locations on the basis of gene expression were visualized through principal component analysis. We used regularized logarithmic transformation (rlog) of the normalized counts for all samples to obtain the principal component analysis so each gene contributes equally to the distance between samples. Volcano plots were obtained in R only highlighting differentially expressed genes with $P < 0.001$ and a $\log_2$-transformed fold change higher or lower than 2 and −2 for upregulated and downregulated genes, respectively.

Preparation of decellularized mouse intestine

Small intestinal tissue was decellularized as previously described[15]. Pieces of decellularized small intestinal ECM (dECM) were washed for 10 min in PBS, plated on a culture dish, and stained with Col-F Collagen Binding Reagent dye (Col-F) (BioSite, 260-6346) overnight at 4 °C. dECM was then washed with fresh PBS, and primed for approximately 30 min with live imaging medium consisting of Advanced DMEM/F12, 1× penicillin–streptomycin, 1× Glutamax (Thermo Fisher Scientific), 10 mM HEPES (Thermo Fisher Scientific), 1× B27 (Life Technologies), 1× N2 (Life Technologies), 1 mM *N*-acetylcysteine (Sigma-Aldrich), 50 ng ml^{-1} of murine recombinant epidermal growth factor (R&D), 100 ng ml^{-1} recombinant murine Noggin (Peprotech), 10 μM Y-27632 (Sigma-Aldrich) and 1 μM jagged-1 peptide (Anaspec). After priming, excess medium was discarded to enable seeding of LGR5$^+$ cells.

Single-cell isolation and FACS

LGR5$^+$ cells were isolated as previously described[20], with a modified protocol to effectively detach epithelium. In brief, longitudinally opened intestine was cut into 5–7 cm pieces, and incubated in 10 mM PBS-EDTA for 30 min. Intestinal pieces were first gently scraped using a microscopy slide to discard villous material and scraped once more to collect crypts.

Live imaging of LGR5$^+$ cells on dECM

LGR5$^+$ cells were stained and washed with 5 μM 647CellTracker (Invitrogen) according to the manufacturer's protocol. Approximately 10,000 cells in 10–20 μl of medium were then seeded on to the scaffold and were allowed to settle for 10 min before adding 10 μl of medium. Additional medium was then carefully introduced in two phases: 20 μl at 20 min after seeding and 260 μl at 30 min after seeding.

Cells were live imaged with a Nikon spinning-disk confocal microscope, using a PlanApo ×10/0.5 NA dry objective and NIS-Elements AR (v.5.02.01; Nikon). A stack of images covering the whole height of the crypt–villus axis was captured with 2.5 μm separation between the images, and the full stack was imaged every 2 min. Cells were imaged for about 4 h and live/dead cells were assessed at the end of imaging by staining with DAPI (Thermo Fisher Scientific, 1 μg ml^{-1}). Col-F was detected by using a 488 nm laser with a 520/30 emission filter, the 647CellTracker was detected using a 640 nm laser with a 685/40 emission filter, and a 405 nm laser with an emission filter 447/60 for DAPI.

Analysis of single-LGR5$^+$-cell migration on dECM

For preprocessing, the images were corrected for *xy* drift, when needed, using the 'Register Virtual Stack Slices' and 'Transform Virtual Stack Slices' plugins in ImageJ. In brief, the bright-field images were used to make a maximum intensity projection over the *z*-levels. Next, drift was registered using with the following parameters: 'Feature extraction model: Translation'; 'Registration model: Translation --no deformation'; 'Save transforms' option selected. Subsequently, the transformations over the time lapse were applied for each of the respective *z*-level on the bright-field and fluorescent images using the 'Transform Virtual Stack Slices' plugin, which were then reassembled into hyperstacks.

Cell tracking was performed with a combination of automatic tracking, using the 'Trackmate' plugin (v.6.0.3)[29] in ImageJ, and manual adjustment of the selected tracks (for example, joining split tracks as needed). The results were then exported for subsequent analysis.

Analysis of the cell tracking results was performed using custom scripts in Python (v.3.10). In brief, each cell was classified on the basis

of its location in *z* (acquired by visual inspection of the decellularized intestinal pieces before the start of the time lapse) into crypt or villus regions. Cell motility was calculated as the Euclidean distance between each time point and its preceding time point. Finally, the results were plotted as the mean and 95% CI, using a polynomial fit (numpy.polyfit, numpy v.1.19.5) for each of the tracks.

In vitro migration assay

Small intestinal organoids from the Lgr5-EGFP-ires-creERT2 × R 26R-confetti mouse were generated and directly induced (that is, before the first passage) with TAT-Cre recombinase (5 µl ml^{-1}, Merck, SCR508). After 5 days in culture both, the LGR5^{+}confetti–RFP^{+} and LGR5^{+}/confetti–YFP^{+} stem cells were sorted (SONY MA900 cell sorter) and plated as single cells[30]. After 7 days of culture, 2,500 or 1,250 LGR5–GFP^{+}confetti–RFP^{+} stem cells and 1,250 CD24^{high}/confetti–YFP^{+} PCs were sorted from these two respective organoid cultures[14] into ultra-low-attachment 96-well round-bottom plates (Sarstedt, 82.1582.001) containing 135 µl of medium. PCs were sorted on the basis of CD24 expression (1:400, Thermo Fisher Scientific, 48-0242-82) and all cells were exposed to live–dead dye (1:200, DRAQ7, Thermo Fischer Scientific, D15105) to sort for living cells. The basic medium[25] was supplemented with either 50% WNT3A CM, IWP2 (2 µM, Tocris, 3533)[31]. After sorting, the plate was left on ice for 15 min and 15 µl of Matrigel was added before 5 min of centrifugation (300*g* with low acceleration and breaking). The fluorescent and bright-field images were acquired every 15 min by a spinning-disk confocal (ImageXpress Micro Confocal) equipped with a ×10/0.45 NA Nikon Plan Apo Lambda objective and live imaging chamber (humidified with sterile water and maintained at 37 °C, 6.4% CO_2). All organoid lines were tested and confirmed to be negative for mycoplasma contamination.

Processing of in vitro migration data

The TrackMate plugin (ImageJ v.2.3.0)[29,32] was used to unbiasedly track the location of individual cells over time (estimated object diameter = 10 µm, linking max distance = 45 µm, gap closing max distance = 15 µm, gap closing max frame gap = 1). CelltrackR[33] (R v.4.1.1), DiPer[34] (Microsoft Excel 2016) and custom made code were used to calculate the mean square displacement, speed and persistence. Replicates with a low number of tracks (<40) or for which the cell density was near confluent were excluded from the analysis, leading to the exclusion of one biological replicate. For each condition, the data are based on three independent biological replicates, each including two to four technical replicates. To calculate the migration speed and directionality of the motile cells, only tracks from motile cells were included (that is, with speed >0.3 µm min^{-1}).

DT treatment

For the LGR5^{+} cell ablation studies, male and female *Lgr5DTR:eGFP* mice received 50 µg kg^{-1} DT in PBS through intraperitoneal injections for 2 days in a row and were euthanized after 24 h, 48 h, 96 h, 7 days and 15 days. Small and large intestines were collected, stained with DAPI and Phalloidin Alexa Fluor 647 (Thermo Fisher Scientific, A22287) and imaged ex vivo.

Statistics

Any a priori sample size calculation could not be performed, as the effect size and the variance was not known before the experiments. No data or animals were excluded, except for in the in vitro migration assay, in which one biological replicate was excluded owing to low number of trackable cells (<40). Owing to differences in crypt morphology, blinding was not possible when comparing the SI and LI. All other comparisons of intravital microscopy experiments and the in vitro migration assay were analysed in a blinded manner. The imaging data were randomized by one researcher and analysed by another researcher. For the analysis of the migration data, the randomization was performed using a custom script in Python and R, and analysed in a blinded manner by the researcher. All *P* values were calculated using two-sided Mann–Whitney *U*-tests in GraphPad Prism v.9 (GraphPad). Details on statistics concerning the mathematical modelling are provided in the Supplementary Notes.

Reporting summary

Further information on research design is available in the Nature Research Reporting Summary linked to this paper.

Data availability

The RNA-seq data are available at the Gene Expression Omnibus (GEO) under accession code GSE194250. All other data are included within the Article and its Extended Data and Supplementary Information and are available at Figshare (https://figshare.com/projects/Azkanaz_et_al_2022_Retrograde_movements_determine_effective_stem_cell_numbers_in_the_intestine/139210). Source data are provided with this paper.

Code availability

The codes and data used for fits, simulations, RNA-seq, in vitro cell migration and single LGR5^{+} cell migration on dECM are available at GitHub (https://github.com/JaccovanRheenenLab/Retrograde_movement_Azkanaz_Nature_2022).

22. Madisen, L. et al. A robust and high-throughput Cre reporting and characterization system for the whole mouse brain. *Nat. Neurosci.* **13**, 133–140 (2010).
23. Ritsma, L. et al. Surgical implantation of an abdominal imaging window for intravital microscopy. *Nat. Protoc.* **8**, 583–594 (2013).
24. McLean, I. W. & Nakane, P. K. Periodate-lysine-paraformaldehyde fixative. A new fixation for immunoelectron microscopy. *J. Histochem. Cytochem.* **22**, 1077–1083 (1974).
25. Sato, T. et al. Single Lgr5 stem cells build crypt-villus structures in vitro without a mesenchymal niche. *Nature* **459**, 262–265 (2009).
26. Jiang, H., Lei, R., Ding, S. W. & Zhu, S. Skewer: a fast and accurate adapter trimmer for next-generation sequencing paired-end reads. *BMC Bioinform.* **15**, 182 (2014).
27. Dobin, A. et al. STAR: ultrafast universal RNA-seq aligner. *Bioinformatics* **29**, 15–21 (2013).
28. Love, M. I., Huber, W. & Anders, S. Moderated estimation of fold change and dispersion for RNA-seq data with DESeq2. *Genome Biol.* **15**, 550 (2014).
29. Tinevez, J. Y. et al. TrackMate: an open and extensible platform for single-particle tracking. *Methods* **115**, 80–90 (2017).
30. Serra, D. et al. Self-organization and symmetry breaking in intestinal organoid development. *Nature* **569**, 66–72 (2019).
31. Miao, Y. et al. Next-generation surrogate Wnts support organoid growth and deconvolute frizzled pleiotropy in vivo. *Cell Stem Cell* **27**, 840–851 (2020).
32. Schindelin, J. et al. Fiji: an open-source platform for biological-image analysis. *Nat. Methods* **9**, 676–682 (2012).
33. Wortel, I. M. N., Dannenberg, K., Berry, J. C., Miller, M. J. & Textor, J. CelltrackR: an R package for fast and flexible analysis of immune cell migration data. Preprint at *bioRxiv* https://doi.org/10.1101/670505 (2019).
34. Gorelik, R. & Gautreau, A. Quantitative and unbiased analysis of directional persistence in cell migration. *Nat. Protoc.* **9**, 1931–1943 (2014).

Acknowledgements We thank the members of the van Rheenen laboratory for reading the manuscript, and the members of the bioimaging, FACS and animal facility of the NKI for experimental support. We acknowledge the staff at the MedH Flow Cytometry core facility, Karolinska Institutet, and LCI facility/Nikon Center of Excellence, Karolinska Institutet. This work was financially supported by the Netherlands Organization of Scientific Research NWO (Veni grant 863.15.011 to S.I.J.E. and Vici grant 09150182110004 to J.v.R.) and the CancerGenomics.nl (Netherlands Organisation for Scientific Research) program (to J.v.R.) the Doctor Josef Steiner Foundation (to J.v.R). B.D.S. acknowledges funding from the Royal Society E.P. Abraham Research Professorship (RP\R1\180165) and the Wellcome Trust (098357/Z/12/Z and 219478/Z/19/Z). B.C.-M. acknowledges the support of the field of excellence 'Complexity of life in basic research and innovation' of the University of Graz. O.J.S. and their laboratory acknowledge CRUK core funding to the CRUK Beatson Institute (A17196 and A31287) and CRUK core funding to the Sansom laboratory (A21139). P.K. and their laboratory are supported by grants from the Swedish Research Council (2018-03078), Cancerfonden (190634), Academy of Finland Centre of Excellence (266869, 304591 and 320185) and the Jane and Aatos Erkko Foundation. P.L. has received funding from the European Research Council (ERC) under the European Union's Horizon 2020 research and innovation programme (grant agreement no. 758617). E.H. acknowledges funding from the European Research Council (ERC) under the European Union's Horizon 2020 research and innovation programme (grant agreement no. 851288).

Author contributions S.I.J.E., L.B., E.H., B.D.S., A.T.W., P.K. and J.v.R. conceived parts of the study. M.A., S.I.J.E., L.B. and S.J.A.L. performed the intravital microscopy experiments with the supervision of H.J.S. and J.v.R. B.C.-M. and E.H. performed the mathematical modelling with input from B.D.S. D.J.H., D.J.F. and O.J.S. provided in situ hybridization, immunohistochemistry

and LGK974-treatment data. A.T.W., S.I., K.A., M.K. and P.K. developed and performed the decellularization experiments and the single-cell motility analysis. K.C.O. and P.L. performed the in vitro cell migration assays. D.L. performed analysis of the in vitro cell migration and sequencing data. F.R.-R. helped with analysing and interpreting sequencing data. M.V. and H.A.M. validated data by qPCR and imaging. All of the authors contributed to writing and have approved the manuscript.

Competing interests The authors declare no competing interests.

Additional information

Supplementary information The online version contains supplementary material available at https://doi.org/10.1038/s41586-022-04962-0.

Correspondence and requests for materials should be addressed to Benjamin D. Simons, Pekka Katajisto, Edouard Hannezo or Jacco van Rheenen.

Peer review information *Nature* thanks Elaine Fuchs, Christina Lo Celso and the other, anonymous, reviewer(s) for their contribution to the peer review of this work.

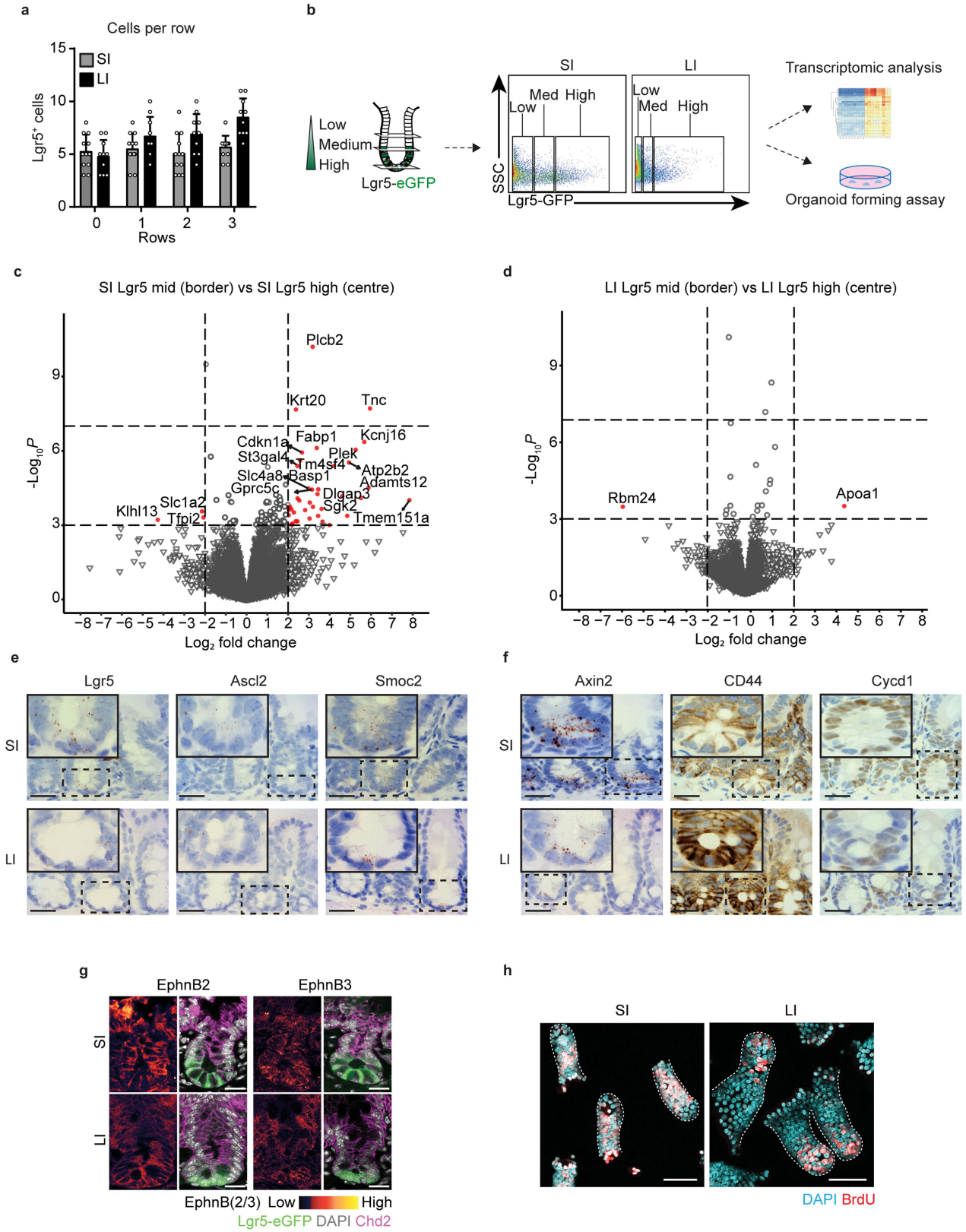

Extended Data Fig. 1 | See next page for caption.

Extended Data Fig. 1 | Crypt characteristics in small and large intestine. **a**, Quantification of the number of LGR5$^+$ cells per position in crypt of SI (n = 12 crypts) and LI (n = 12 crypts) in Lgr5eGFP-Ires-CreERT2 mice. Mean +/− SD are plotted **b**, Schematic representation of experimental setup for RNA-seq and organoid forming assay. **c**,**d**, Volcano plots showing log2 fold-change (x-axis) and -Log_{10} p-value (y-axis) of genes differentially expressed between LGR5$^+$ cells with medium intensity (border) and LGR5$^+$ cells with high intensity (centre). Genes that were significantly altered in border compared with centre LGR5$^+$ cells are highlighted in red (Log_2 fold change >2, -Log_{10} p-value <0.001) in SI (**c**) and LI (**d**), n = 4 mice for each condition. **e**, Stem cell markers (*Lgr5, Ascl2* and *Smoc2*) *in situ* hybridization (ISH) in C57/B6 mouse SI (top) and LI (bottom) crypts, n = 4 mice. Scale bar, 100 µm. **f**, Wnt targets (AXIN2, CD44, CYCD1) ISH and immunohistochemistry (IHC) in C57/B6 mouse SI (top) and LI (bottom) crypts, n = 4 mice. Scale bar, 100 µm. **g**, Immunofluorescence (IF) staining of Ephrin B2 and Ephrin B3 in C57/B6 mouse SI (top) and LI (bottom) crypts, n = 3 experiments. Scale bar, 20 µm. **h**, Confocal images of isolated crypts (dotted outline) of SI (left), and LI (right), proliferating cells were identified by BrdU incorporation upon 2-hour pulse (red). Nuclei were labelled using DAPI (blue), n = 10 experiments. Scale bar, 50 µm.

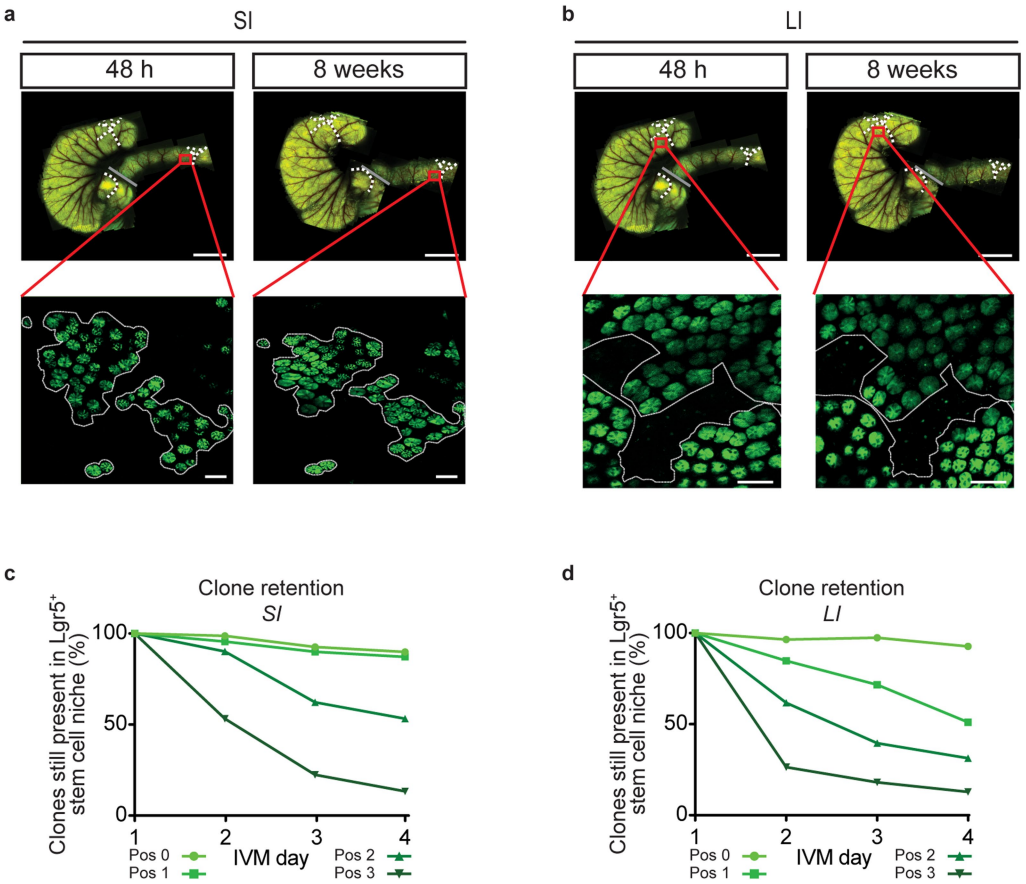

Extended Data Fig. 2 | Visualizing effective stem cells by intravital imaging in small and large intestine. a,b, Representative overview images 48 h (left) and 8 weeks (right) after tracing in Lgr5eGFP-Ires-CreERT2 mice from 6 independent experiments. Dotted lines represent same areas. Grey lines indicate SI LI boundary. Lower pictures represent intravital images showing crypt patterns (LGR5-eGFP in green) at 48h and 8w after tracing in SI (**a**) and LI (**b**). Dotted lines are examples of retraced patchy LGR5$^+$ areas. Scale bar, 5 mm (top), 100 µm (bottom) from 5 independent experiments. **c**,**d**, Quantification of retention within the LGR5$^+$ zone of clones starting from different positions in the niche (shades of green) in SI (**c**) and LI (**d**) as followed by IVM. SI: n = 305 clones in 9 mice; LI: n = 311 clones in 5 mice (see Ext. Data Fig. 3–6).

Extended Data Fig. 3 | Short-term evolution of clones in SI (1). Presence in centre (light green) and border (dark green) of individual clones in Lgr5eGFP-Ires-CreERT2; R26-Confetti mice followed by short-term IVM in SI is plotted over time (squares represent individual clones, with a bar per day). Plotted are clones starting and remaining in the centre (top panel), starting and remaining in centre while spreading to border (middle panel) and starting in the centre and transferring to border (bottom panel).

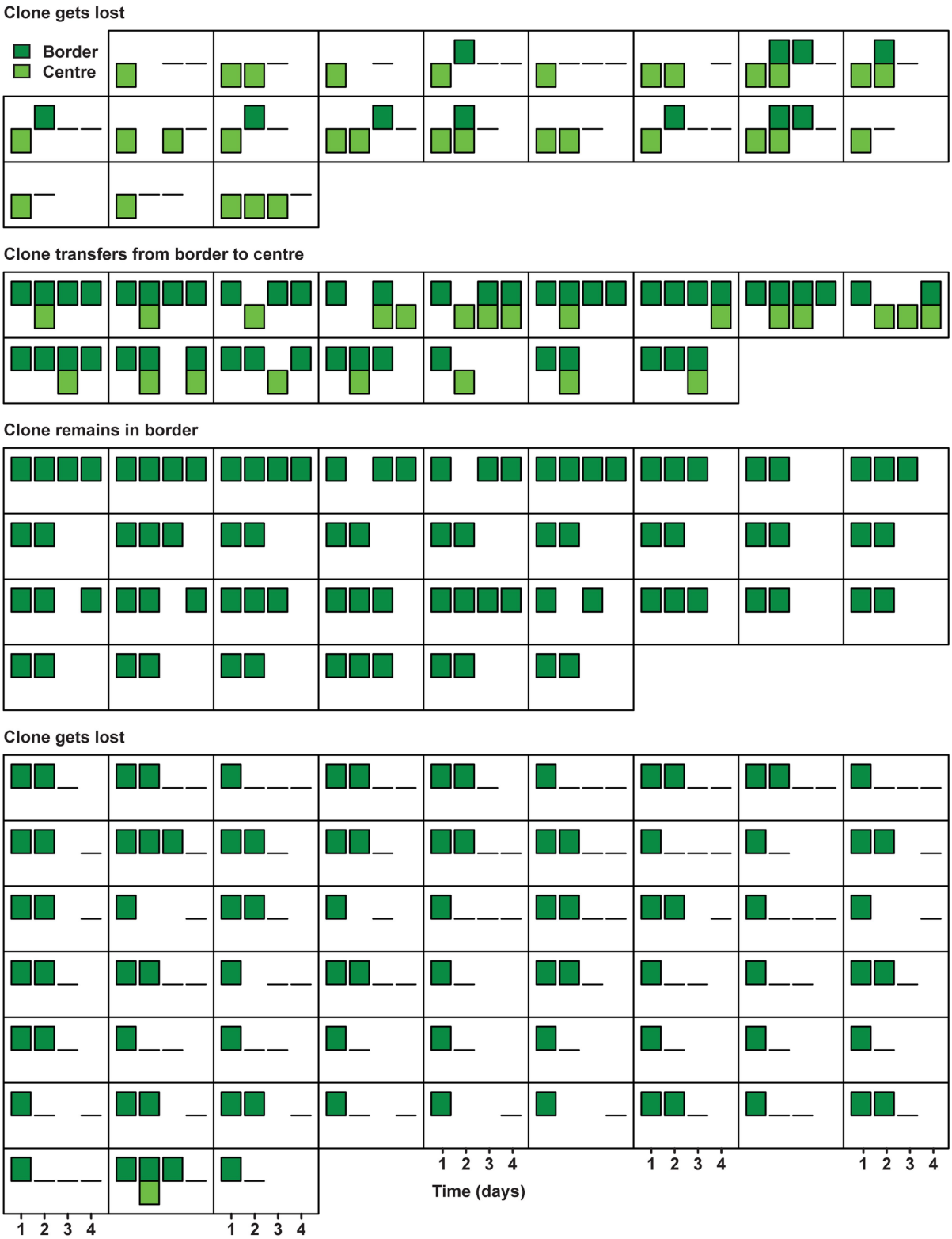

Extended Data Fig. 4 | Short-term evolution of clones in SI (2). Presence in centre (light green) and border (dark green) of individual clones in Lgr5eGFP-Ires-CreERT2; R26-Confetti mice followed by short-term IVM in SI are plotted over time (represent individual clones with a bar per day). Plotted are clones starting in the centre and getting lost (top panel), starting in border and transferring to centre (second panel), starting in border and remaining in border, and starting in border before getting lost.

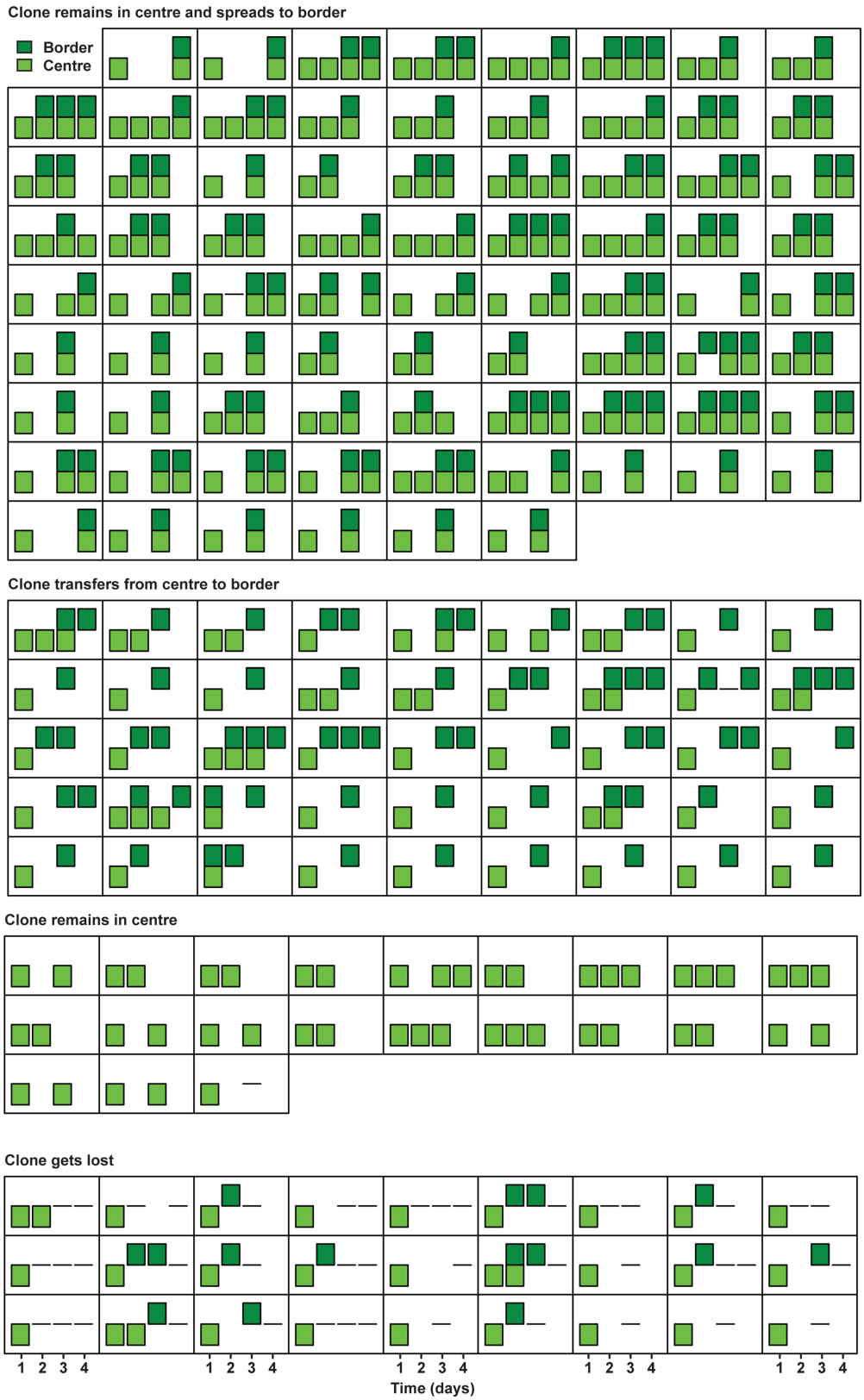

Extended Data Fig. 5 | Short-term evolution of clones in LI (1). Presence in centre (light green) and border (dark green) of individual clones in Lgr5eGFP-Ires-CreERT2; R26-Confetti mice followed by short-term IVM in LI are plotted over time (squares represent individual clones with a bar per day). Plotted are clones starting and remaining in the centre while spreading to border (top panel), starting in the centre and transferring to border (second panel), starting and remaining in centre without spreading to border (third panel) and starting in the centre before getting lost from the niche (bottom panel).

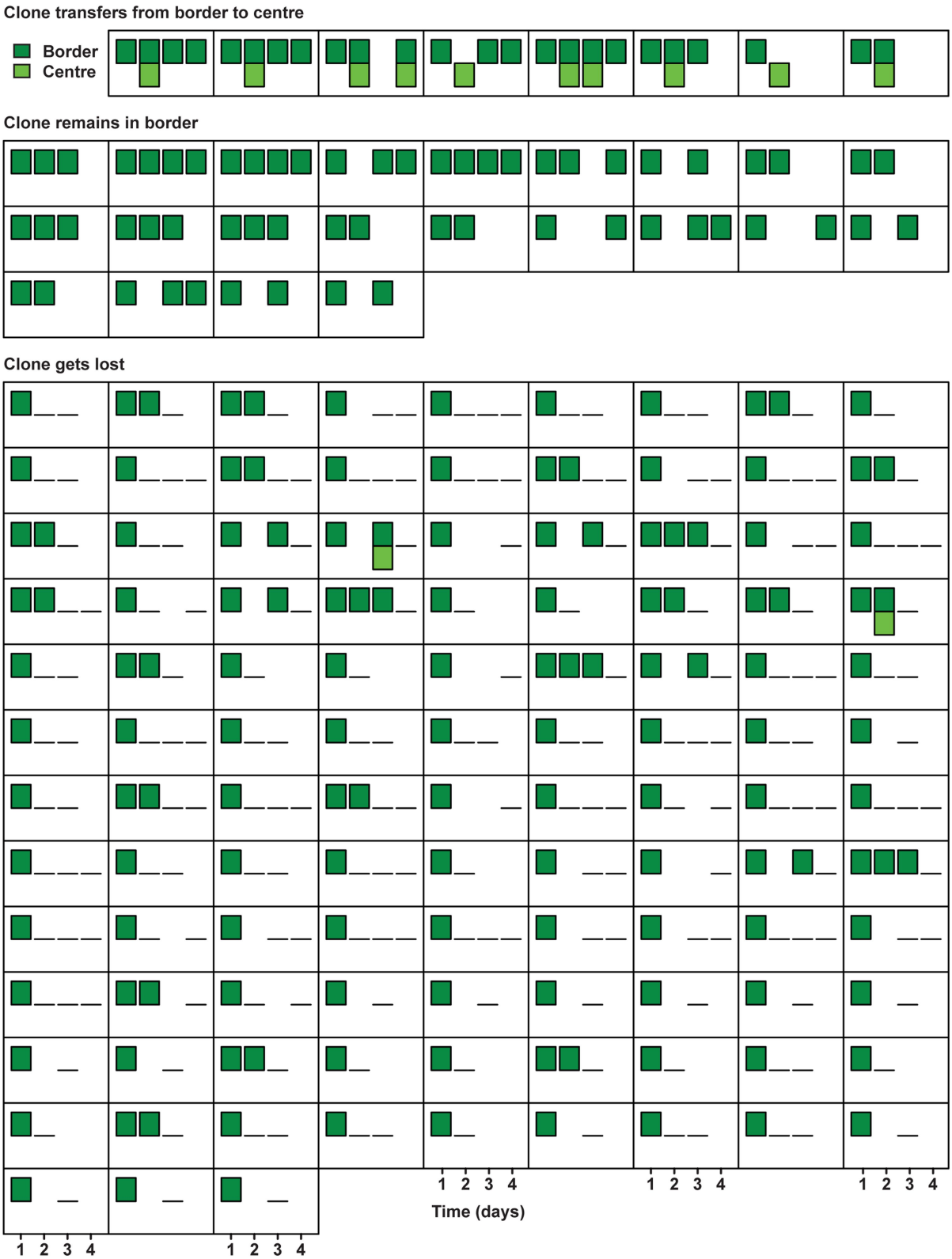

Extended Data Fig. 6 | Short-term evolution of clones in LI (2). Presence in centre (light green) and border (dark green) of individual clones in Lgr5eGFP-Ires-CreERT2; R26-Confetti mice followed by short-term IVM in LI are plotted over time (squares represent individual clones with a bar per day). Clones are Plotted are clones starting in border and transferring to centre (top panel), starting in border and remaining there (second panel), starting in border before getting lost (bottom panel).

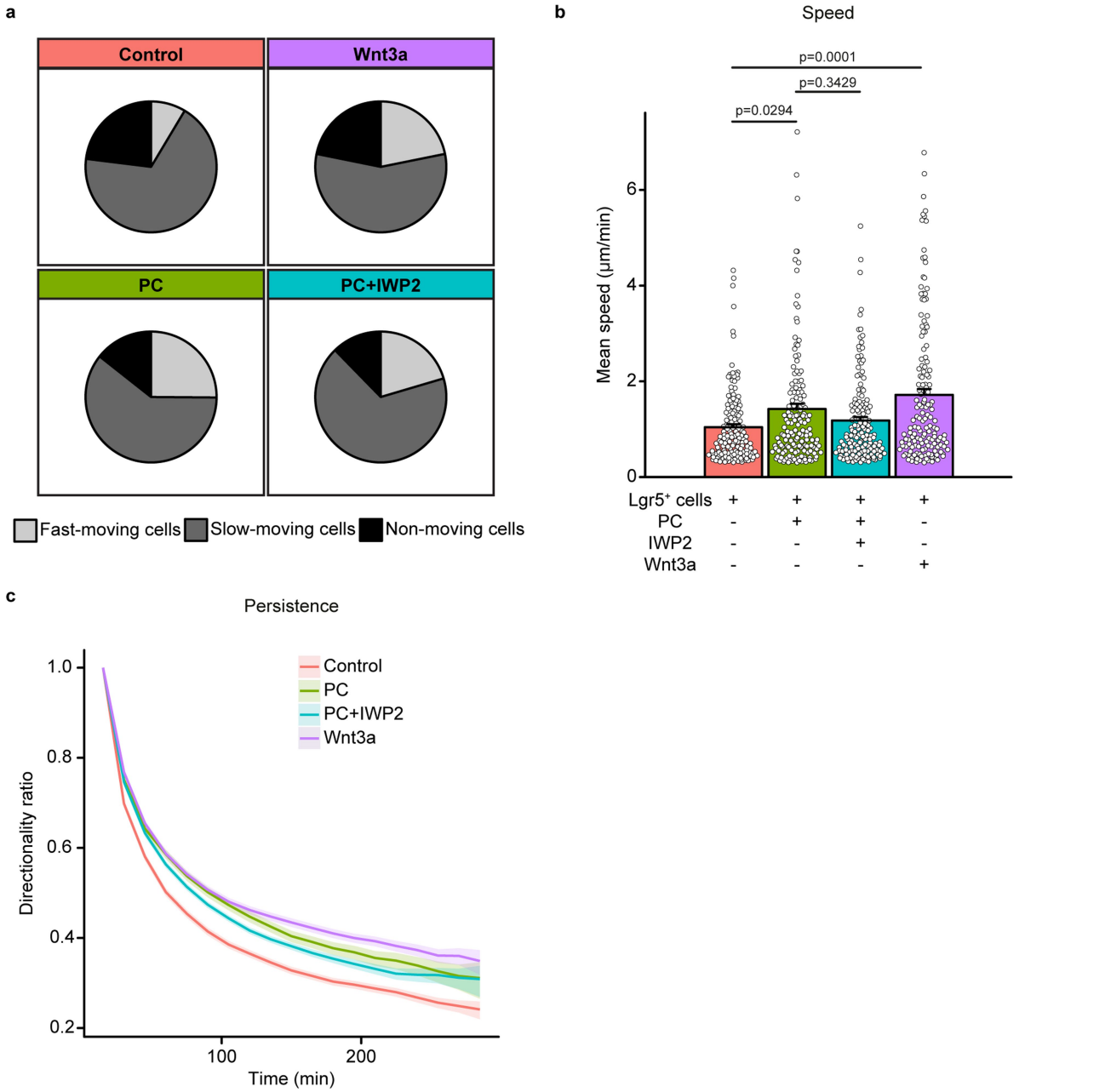

Extended Data Fig. 7 | Wnt enhances motility *in vitro*. **a**, Percentage of fast-moving (>2 µm/min), slow-moving (0.3-2 µm/min) and non-moving (<0.3 µm/min) LGR5$^+$ cells. The imaged LGR5$^+$ cells were isolated from Lgr5-EGFP-ires-creERT2;R26R-confetti organoids and exposed to (I) control medium (n = 408 cells), (II) medium supplemented with Wnt3a (n = 582 cells), (III) medium supplemented with Paneth cells (PC) (n = 418 cells), or (IV) medium supplemented with PC and Wnt inhibitor (IWP2) (n = 431 cells) in Matrigel from 3 independent biological replicates. **b**,**c** Speed (**b**) and directionality ratio (persistence) over time calculated as mean displacement/length of the trajectory. Significance was determined by a two-sided Mann-Whitney test. (**c**) of single LGR5$^+$ cells in control medium, medium supplemented with Wnt3a, co-culture with PC and co-culture PC with IWP2. Shown are n = 150 random cell tracks of LGR5$^+$ cells from 2 independent organoid lines, 50 from each of 3 independent biological replicates. Each point represents the mean value of each track. Shown are mean ± SEM.

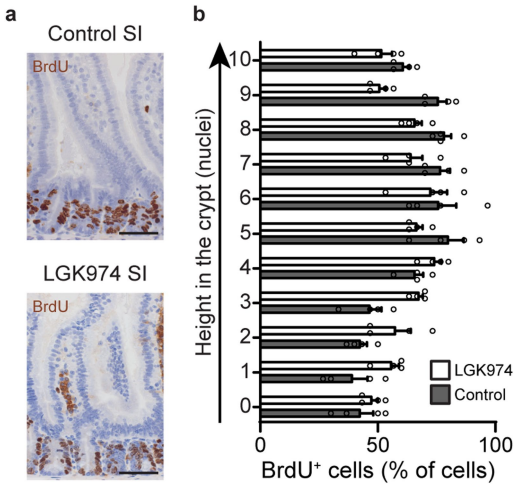

Extended Data Fig. 8 | The effect of LGK974 on stem cell dynamics in small intestinal crypts. a, Representative image of 2h BrdU pulse in SI crypts of control and LGK974-treated mice. Scale bar, 50 µm. **b**, Quantification of cells positive for BrdU per position in SI crypts of control and LGK974-treated mice. Of note, position is based on nuclei count which does not discriminate between stem cells and PCs, and the LGR5+ zone ends around nuclear position 6-8. Mean +/− SEM are plotted. (n = 120 crypts examined over 4 independent experiments from 4 mice, 30 crypts per mouse).

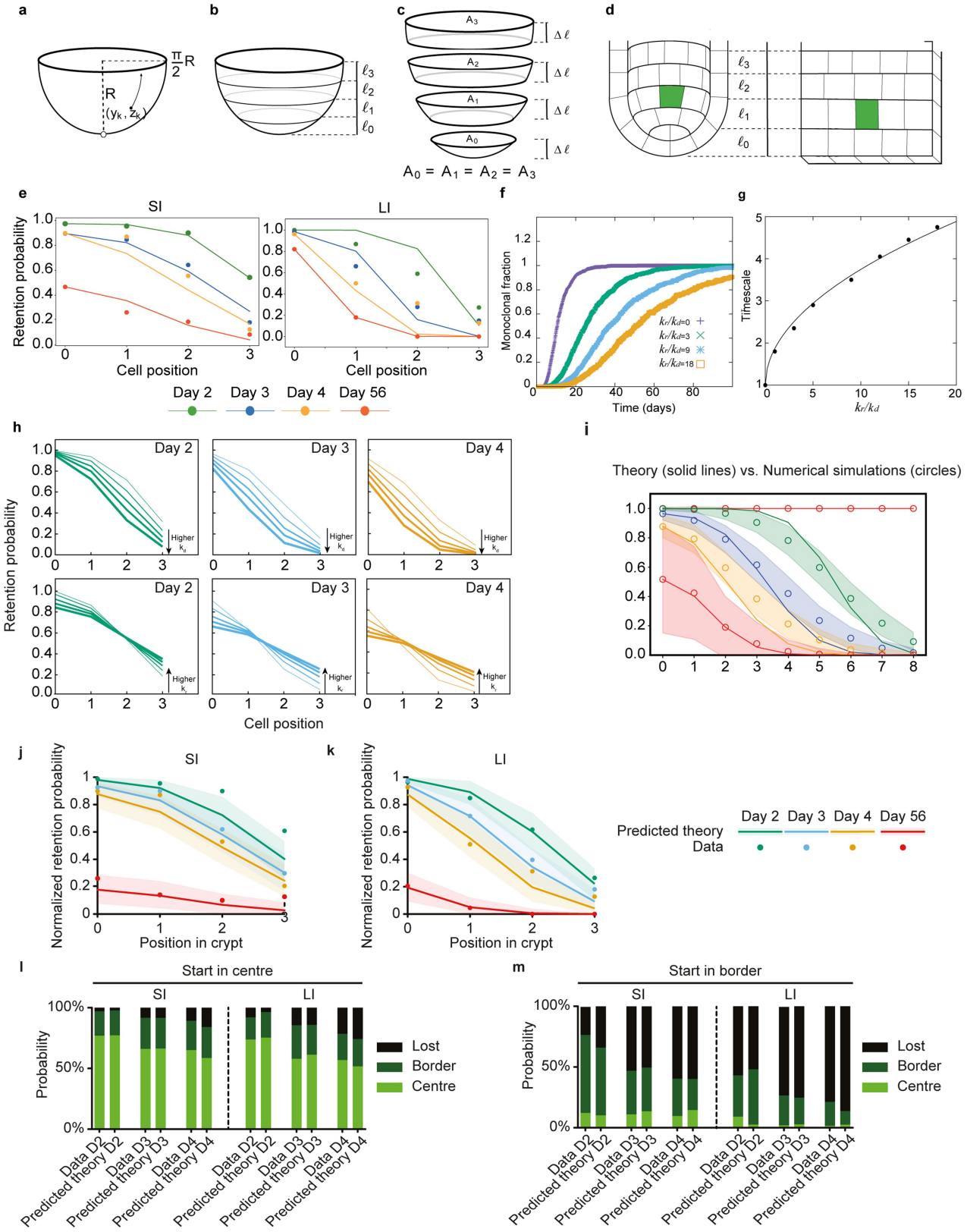

Extended Data Fig. 9 | See next page for caption.

Extended Data Fig. 9 | Biophysical modelling of stochastic conveyor belt dynamics in small versus large intestine. a, An intestinal crypt is abstracted as a hemispherical surface. A cell experiences net upwards force due to the divisions taking place at lower positions, together with stochastic repositioning events. **b**, This hemispheric region can be segmented by cuts at different heights, $\ell 0, \ell 1, \ell 2, \ell 3$. **c**, If the sections defined by these cuts are of the same width, $\Delta\ell$, then the area of each is the same, which provides an explanation for the near-constant number of LGR5+ cell at each position. **d**, This allows us to approximate the system as consecutive layers of cells on a cylinder. **e**, Analytical solutions for the stochastic conveyor belt model (probability of clone retention per time). Left (resp. right) plot shows the retention probability as a function of the starting position of the mother cell of the lineage for the SI (resp. LI). Points show the experimental data for wild-type (same as Fig. 3), lines are the prediction of the stochastic conveyer belt dynamics given by equation (1.3) of the SI Theory Note. In both panels, the color scheme is: Green, 2 days, Blue, 3 days, orange, 4 days, and red 56 days post-labelling. **f**, Average monoclonal conversion in crypts for different values of $kr\,kd$; and rescaled time it takes to convert. **g**, Corresponding time of conversion as a function of $kr\,kd$ (points) which are very well fitted by a square root (lines), showing that the time increases close to linearly with $\sqrt{kr/kd}$. **h**, Sensitivity analysis of the 2D numerical simulations. Top, effect of increasing values of the division rate k_d on the resulting short-term clonal retention dynamics as a function of initial cell positions at days 2, 3 and 4 (left, middle and right panel respectively), for constant $k_r = 0.25$ (LI best-fit value). Increasing thickness of the lines indicate increasing division rate (or alternatively decreasing division time: 2.3, 1.7, 1.4, 1.2, 0.9 divisions per day respectively – note that the middle curve thus corresponds to the value of 1.4 divisions per day used in the main text). Bottom, Effect of increasing values of the division rate k_r on the resulting short-term clonal retention dynamics as a function of initial cell positions at days 2, 3 and 4 (left, middle and right panel respectively), for constant $k_d = 0.5$ (LI best-fit value). Increasing thickness of the lines indicate increasing $k_r = 0.25, 1, 2, 3, 4$ (note that the first curve thus corresponds to the best fit value used in the main text). **i**, Comparison between 1D analytical theory (solid lines) and 2D simulations (circles) for the clonal retention probability (y-axis, parameters chosen as kr = 2, 1/kd = 1.2 divisions per day) as a function of initial starting position for the clone (x-axis) and time (colors red, green, blue, yellow and red indicating resp. day 1, day 2, day 3, day 4 and day 56). Dashed region indicates the standard deviation observed in the simulations for the respective simulation time. **j**,**k**, Normalized probability of retention in LGR5+ zone for different starting positions over time in SI (f; n = 305 clones in 9 mice) and LI (g; n = 334 clones in 5 mice) predicted by model (solid lines and shaded intervals, mean with 95% confidence interval) and experimental data (dots). **l**,**m**, Probability of presence in centre, border or loss of centre-starting (left) and border-starting clones (right) over time in SI (h, n = 305 clones in 9 mice) and LI (I, n = 311 clones in 5 mice), comparing data (left bar) and theory (right bar).

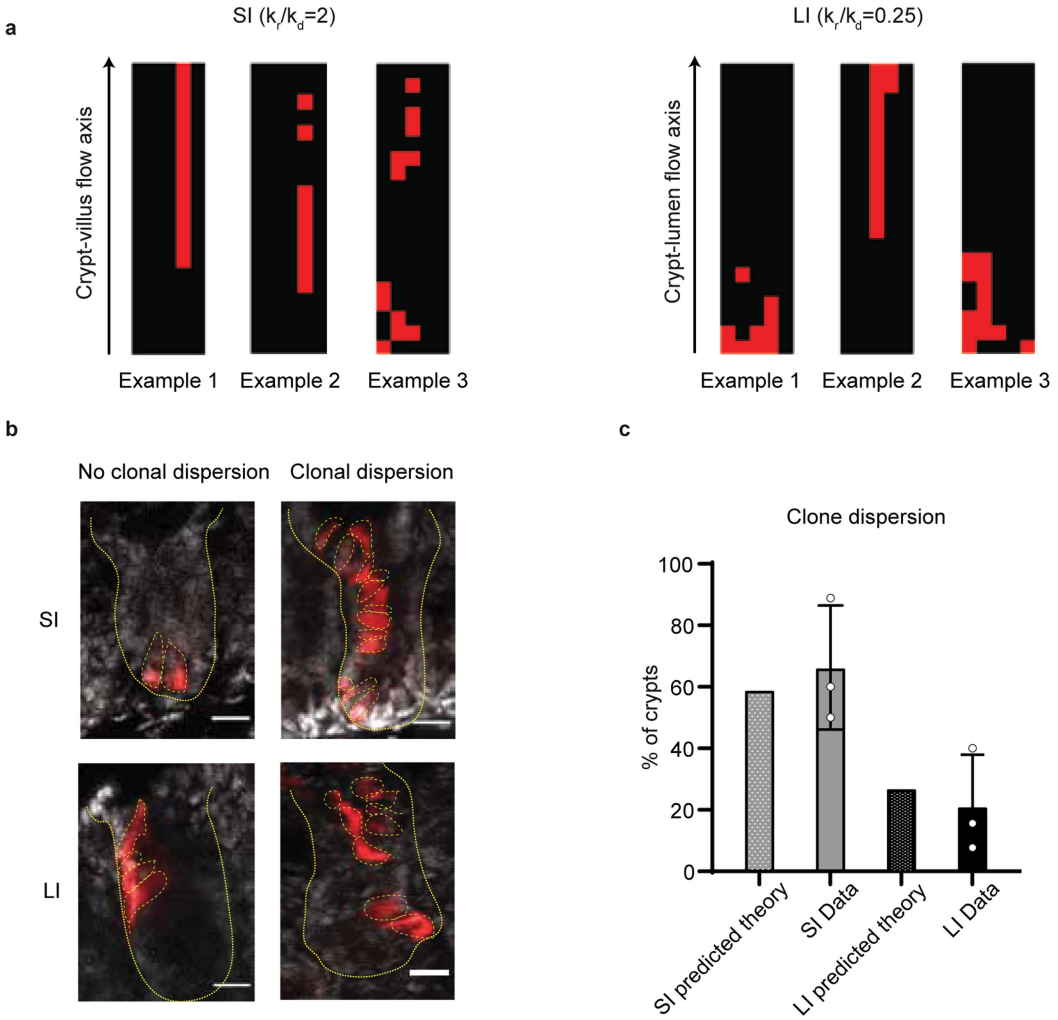

Extended Data Fig. 10 | Clonal dispersion in small and large intestine. **a**, Typical outputs of 2D numerical simulations of a single clonal labelling event (labelled cells indicated in red) for the parameter set extracted from SI (left) and LI (right) data. As expected, larger values of k_r result in a higher probability of clonal fragmentation (defined as the probability of a given clone displaying two fragments separated by a row of clonally non-labelled cells, see SI Note for details on the simulations). **b**, SI (top) and LI (bottom) crypts with sparse lineage-tracing experiment, where a single lineage (red here, induced and imaged 7 days post induction) can be observed. Clonal dispersion due to cell rearrangements is either observed (right) or not (left). Scale bar, 20 µm. **c**, Probability of clonal fragmentation in SI and LI (data shown in grey (SI) and black (LI), theory in dotted bars extracted from the parameters in panel a), showing good agreement. Data is based on n = 3 mice (20 crypts for SI and 55 crypts for LI). Each data point represents percentage of clonal dispersed crypts in one mouse, and bars show mean +/− SD.

nature portfolio

Corresponding author(s): Benjamin Simons, Pekka Katajisto, Edouard Hannezo and Jacco van Rheenen

Last updated by author(s): May 13, 2022

Reporting Summary

Nature Portfolio wishes to improve the reproducibility of the work that we publish. This form provides structure for consistency and transparency in reporting. For further information on Nature Portfolio policies, see our Editorial Policies and the Editorial Policy Checklist.

Statistics

For all statistical analyses, confirm that the following items are present in the figure legend, table legend, main text, or Methods section.

n/a	Confirmed	
☐	☒	The exact sample size (*n*) for each experimental group/condition, given as a discrete number and unit of measurement
☐	☒	A statement on whether measurements were taken from distinct samples or whether the same sample was measured repeatedly
☐	☒	The statistical test(s) used AND whether they are one- or two-sided *Only common tests should be described solely by name; describe more complex techniques in the Methods section.*
☒	☐	A description of all covariates tested
☒	☐	A description of any assumptions or corrections, such as tests of normality and adjustment for multiple comparisons
☐	☒	A full description of the statistical parameters including central tendency (e.g. means) or other basic estimates (e.g. regression coefficient) AND variation (e.g. standard deviation) or associated estimates of uncertainty (e.g. confidence intervals)
☐	☒	For null hypothesis testing, the test statistic (e.g. *F*, *t*, *r*) with confidence intervals, effect sizes, degrees of freedom and *P* value noted *Give P values as exact values whenever suitable.*
☒	☐	For Bayesian analysis, information on the choice of priors and Markov chain Monte Carlo settings
☒	☐	For hierarchical and complex designs, identification of the appropriate level for tests and full reporting of outcomes
☒	☐	Estimates of effect sizes (e.g. Cohen's *d*, Pearson's *r*), indicating how they were calculated

Our web collection on statistics for biologists contains articles on many of the points above.

Software and code

Policy information about availability of computer code

Data collection	scipy.optimize Python (version 3.10) library was used
Data analysis	We used Python software (v 3.10), Fiji/ImageJ (v 2.3.0) ("Register Virtual Stack Slices", "Transform Virtual Stack Slices" and "Trackmate" plugins) GraphPad Prism(v 9), FlowJo (v10.6.1), Illumina bcl2fastq (version 2.20), Skewer (version 0.2.2), STAR (version 2.5.2b), DeSeq2 (version 1.34 in Bioconductor 3.14), R (version 4.1.1), numpy.polyfit (numpy version 1.19.5), CelltrackR, DiPer and custom-made codes for analysis. The codes and data used for fits, simulations, RNAseq, in vitro cell migration and single Lgr5+ cell migration on dECM are available in GitHub (https://github.com/JaccovanRheenenLab/Retrograde_movement_Azkanaz_Nature_2022).

For manuscripts utilizing custom algorithms or software that are central to the research but not yet described in published literature, software must be made available to editors and reviewers. We strongly encourage code deposition in a community repository (e.g. GitHub). See the Nature Portfolio guidelines for submitting code & software for further information.

Data

Policy information about availability of data

All manuscripts must include a data availability statement. This statement should provide the following information, where applicable:

- Accession codes, unique identifiers, or web links for publicly available datasets
- A description of any restrictions on data availability
- For clinical datasets or third party data, please ensure that the statement adheres to our policy

TThe RNA sequencing data is available through the Gene Expression Omnibus (GEO) with the accession code GSE194250. All other data are included within the paper, Extended Data and Supplementary Information and are available through the online data sharing platform Figshare: https://figshare.com/projects/

Azkanaz_et_al_2022_Retrograde_movements_determine_effective_stem_cell_numbers_in_the_intestine/139210. Source Data for all figures are provided with this paper.

Field-specific reporting

Please select the one below that is the best fit for your research. If you are not sure, read the appropriate sections before making your selection.

☒ Life sciences ☐ Behavioural & social sciences ☐ Ecological, evolutionary & environmental sciences

For a reference copy of the document with all sections, see nature.com/documents/nr-reporting-summary-flat.pdf

Life sciences study design

All studies must disclose on these points even when the disclosure is negative.

Sample size

For in vivo experiments, at least 3 animals were used per condition.
-> we performed the intravital imaging (both short and long-term) in >3 animals before we performed the analysis and the comparison with the mathematical model as a pilot. These numbers were enough as it provided us with enough clones (>75) to analyze and to compare the experimental data with the theoretical model.
-> for static lineage tracing, previous papers have used one mouse to determine clonal dynamics. We determined a sample size of >3 mice per time point to do statistics.

For in vitro and ex-vivo experiments, no statistical methods were used to predetermine sample size estimates. Sample size was determined to be adequate based on the magnitude and consistency of measurable differences between groups and based on previous studies with a similar study design.

For ex vivo analysis of stem cell numbers, Lgr5-GFP intensity, crypt dimensions, clone dispersion or proliferation, >10 separate crypts were quantified as done previously (Bruens et al. Cell Reports 2021; Ritsma et al. Nature 2014).
For RNA-seq and organoid forming assay, Lgr5+ cells were isolated from at least 3 animals per group as done previously (van der Flier et al. Cell, 2009; Sato et al. Nature 2011) .

For in vitro migration assay, 150 random cell tracks of Lgr5+ cells from 2 independent organoid lines, 50 from each of 3 independent biological replicates were used for the analysis of speed, persistence and mean square displacement according to (Gorelik et al. Nature protocols, 2014; Wortel et al. BioRxiv, 2019).

For the decellularized intestine experiment, since this concerned a new experimental setup, the variation was unknown prior to the experiment. Based on our experience with imaging experiments, we estimated that we need to acquire 150 or more cells from 3 independent experiments to be able to measure significant differences between experimental groups. In this study, n=150-200 cell tracks on 3 decellularized mouse intestines for each control (vehicle) and LGK974 treated group.

Of note, for most experiment (except for short-term intravital imaging) we could analyze both the small and large intestine from the same animal which served as an internal control and coupled data.

Data exclusions

No data or animals were excluded, except for the in vitro migration assay, where one biological replicate was excluded due to low number of trackable cells (<40).

Replication

All experiments were reproducible.
- Long-term intravital imaging was performed in 3 cohorts of 2 mice (Fig. 2)
- Short-term intravital imaging was performed in >4 mice (Fig. 2).
  -> Short-term intravital imaging of SI yielded the same results as in Ritsma et al. 2014, Nature.
- Static tracing was performed in >3 mice per time point (Fig. 4).
  -> Small and large intestine were analyzed from the same mouse, yielding coupled data.
- RNA-seq, organoid forming assay, decellularized intestine experiment, in vitro migration assay and Lgr5+ ablation experiment were performed in at least 3 biological replicates and yielded in each time similar results.

Moreover,
- Short- and long-term intravital imaging data were analyzed by 3 researchers (S.I.J.S., L.B. and M.A.).
- Experiments have been performed both at the Hubrecht Institute and the Netherlands Cancer Institute, yielding the same results.
- Short and long-term intravital imaging was performed by 4 researchers (S.I.J.S., L.B., S.J.A.L. and M.A.).
- RNA-seq data were analyzed by 2 researchers (F.R.R. and D.L.).
- Lgr5+ ablation experiment was analyzed by 2 researchers (L.B. and M.A.)

Randomization

In many experiments, small and large intestine were taken from the same mouse.

For experiments where this was not possible (short-term intravital imaging [Fig 2] or LGK treatment), either males or females of the same litter were randomly assigned to each condition.

The imaging data were randomized by one researcher and analyzed by another researcher.

For in vitro migration assay, 150 random cell tracks of Lgr5+ cells, 50 from each of 3 independent biological replicates were used for the analysis of speed, persistence and mean square displacement.

Blinding

Due to differences in crypt morphology, blinding was not possible when comparing small and large intestine.

All other comparisons of intravital microscopy experiments and the in vitro migration assay were analyzed in a blinded fashion. The imaging data were randomized by one researcher and analyzed by another researcher.

Reporting for specific materials, systems and methods

We require information from authors about some types of materials, experimental systems and methods used in many studies. Here, indicate whether each material, system or method listed is relevant to your study. If you are not sure if a list item applies to your research, read the appropriate section before selecting a response.

Materials & experimental systems

n/a	Involved in the study
☐	☒ Antibodies
☐	☒ Eukaryotic cell lines
☒	☐ Palaeontology and archaeology
☐	☒ Animals and other organisms
☒	☐ Human research participants
☒	☐ Clinical data
☒	☐ Dual use research of concern

Methods

n/a	Involved in the study
☒	☐ ChIP-seq
☐	☒ Flow cytometry
☒	☐ MRI-based neuroimaging

Antibodies

Antibodies used

Antibodies and RNA probes were extensively validated by the providers and confirmed by the authors for specific localization. anti-GFP (goat, Abcam, cat. no. ab6673), anti-BrdU (rat, Abcam, cat. no. 6326), anti phospho-Histone H3 (Millipore, 06-570), anti-Ephrin B2 (R&D system, AF467), anti-Ephrin B3 (R&D system, AF432), anti-CD44 (1:50 BD Biosciences #550538) and anti-Cyclin D1 (1:50 Dako #M3635). In situ hybridisation for Lgr5 (#312178), Smoc2 (#318548), Ascl2 (#412218) and Axin2 (#400338) mRNA (all from Advanced Cell Diagnostics)
Seconday antibodies: Donkey anti-Goat IgG (H+L) Cross-Adsorbed Secondary antibody, Alexa Fluor 488 (Cat# A-11055), Donkey anti-Rabbit IgG (H+L) Highly Cross-Adsorbed Secondary Antibody, Alexa Fluor 568 (Cat# A-10042), Chicken anti-Rabbit IgG (H+L) Cross-Adsorbed Secondary Antibody, Alexa Fluor 647 (Cat#A-21443)

Validation

All antibodies were validated for use in the assay and species under study by the suppliers and are commonly used for IF and/or IHC (see company websites and exemplary citations below).
Anti-GFP: goat, Abcam, cat. no. ab6673. https://www.abcam.com/gfp-antibody-ab6673.html. Maruno T et al. Elife 10:N/A (2021).

Anti-BrdU: rat, Abcam, cat. no. 6326. https://www.abcam.com/brdu-antibody-bu175-icr1-proliferation-marker-ab6326.html. Udugama M et al. Nat Commun 12:2584 (2021).

Anti phospho-Histone H3: Millipore, 06-570. https://www.merckmillipore.com/NL/en/product/Anti-phospho-Histone-H3-Ser10-Antibody-Mitosis-Marker,MM_NF-06-570. Otsuki et al., Science 360(6384):99-102 (2018).

Anti-Ephrin B2: R&D system, AF467, https://www.rndsystems.com/products/human-mouse-ephb2-antibody_af467. Washburn et al. Nat Commun 11(1):570 (2020).

Anti-Ephrin B3: R&D system, AF432, https://www.rndsystems.com/products/human-ephrin-b3-antibody_af395#product-citations. Yang et al., J. Biol. Chem. 281(43):32574-86 (2006)

Anti-CD44: BD Biosciences #550538, https://www.bdbiosciences.com/en-eu/products/reagents/flow-cytometry-reagents/research-reagents/single-color-antibodies-ruo/purified-rat-anti-mouse-cd44.550538. Bendelac A. Curr Opin Immunol. 7(3):367-374 (1995).

Anti-Cyclin D1: Dako #M3635, https://www.citeab.com/antibodies/2414832-m3642-cyclin-d1-concentrate. Peurala et al., Breast Cancer Res. 15(1):R5 (2013).

In situ hybridisation for Lgr5 (#312178), Smoc2 (#318548), Ascl2 (#412218) and Axin2 (#400338) mRNA (all from Advanced Cell Diagnostics). https://acdbio.com/

Donkey anti-Goat IgG (H+L) Cross-Adsorbed Secondary antibody, Alexa Fluor 488: Invitrogen Cat# A-11055, https://www.thermofisher.com/antibody/product/Donkey-anti-Goat-IgG-H-L-Cross-Adsorbed-Secondary-Antibody-Polyclonal/A-11055.

Donkey anti-Rabbit IgG (H+L) Highly Cross-Adsorbed Secondary Antibody, Alexa Fluor 568: Invitrogen Cat# A-10042, https://www.thermofisher.com/antibody/product/Donkey-anti-Rabbit-IgG-H-L-Highly-Cross-Adsorbed-Secondary-Antibody-Polyclonal/A10042.

Chicken anti-Rabbit IgG (H+L) Cross-Adsorbed Secondary Antibody, Alexa Fluor 647: Invitrogen Cat#A-21443, https://www.citeab.com/antibodies/2401323-a-21443-chicken-anti-rabbit-igg-h-l-cross-adsorbed.

Eukaryotic cell lines

Policy information about cell lines

Cell line source(s)	Small intestinal organoids from 2 Lgr5-EGFP-ires-creERT2 × R26R-confetti mice were established in the lab of Prisca Liberali and directly induced (i.e., before the first passage) with TAT-Cre recombinase (5uL/mL, MERCK #SCR508).
Authentication	The culture conditions select for intestinal cells (Sato et al, Nature 2011). Intestinal stem cell identity was validated by visualizing Lgr5-eGFP expression.
Mycoplasma contamination	All organoid lines were tested and confirmed negative for mycoplasma contamination.
Commonly misidentified lines (See ICLAC register)	No commonly misidentified cell lines were used.

Animals and other organisms

Policy information about studies involving animals; ARRIVE guidelines recommended for reporting animal research

Laboratory animals	Lgr5eGFP-Ires-CreERT2/R26-Confetti and Lgr5eGFP-ires-CreERT2/LSL-tdTomato mice in mixed or C57/B6 background were used for lineage tracing experiments to compare small and large intestine. Mice entered the study between 8 and 52 weeks of age, both males and females. References per mouse strain: Lgr5eGFP-Ires-CreERT2 -> Barker, N. et al. Identification of stem cells in small intestine and colon by marker gene Lgr5. Nature 449, 1003–1007 (2007). R26-Confetti -> Snippert, H. J. et al. Intestinal crypt homeostasis results from neutral competition between symmetrically dividing Lgr5 stem cells. Cell 143, 134–144 (2010). LSL-tdTomato -> Madisen, L. et al. A robust and high-throughput Cre reporting and characterization system for the whole mouse brain. Nat. Neurosci. 13, 133–140 (2010). Lgr5-DTR-GFP -> Tian, H. et al. A reserve stem cell population in small intestine renders Lgr5-positive cells dispensable. Nature 478, 255-259, doi:10.1038/nature10408 (2011).
Wild animals	No wild animals were used in the study.
Field-collected samples	No field collected samples were used in the study.
Ethics oversight	All experiments were carried out in accordance with the guidelines of and are approved by the animal welfare committee of the Netherlands Cancer Institute and Hubrecht Institute (KNAW)

Note that full information on the approval of the study protocol must also be provided in the manuscript.

Flow Cytometry

Plots

Confirm that:

☒ The axis labels state the marker and fluorochrome used (e.g. CD4-FITC).

☒ The axis scales are clearly visible. Include numbers along axes only for bottom left plot of group (a 'group' is an analysis of identical markers).

☒ All plots are contour plots with outliers or pseudocolor plots.

☒ A numerical value for number of cells or percentage (with statistics) is provided.

Methodology

Sample preparation	To obtain single cells, crypts were treated with TrypLE (Life Technology) supplemented with 30 µg/mL DNaseI (Sigma) and Y-27632 (10 µM) (incubation at 37 °C for 30 minutes). Dissociated cells were filtrated by 100-µm cell strainer (Greiner Bio-One), and cells were resuspended and incubated with antibodies for 30 minutes on ice in 1 mL PBS containing FCS 5%, EDTA 5mM (Accugene, Lonza), B27 2% (Thermo Fisher Scientific, cat. no. 17504-044), N-acetylcysteine 1.25 mM (Sigma-Aldrich, cat. no. A9165), mEGF 50 ng/ml (Peprotech, cat. no. 315-09), Noggin and R-spondin1 both 10% (conditioned medium prepared in house), Y-27632 (1 µM) and 4 µg/mL DNaseI (Sigma). The cell suspension was filtered by 70-µm cell strainer (Celltrix) and subjected to flow cytometry
Instrument	FACS Aria Fusion (BD Biosciences)

Software	FlowJo 10.6.1 (https://www.flowjo.com/).
Cell population abundance	Of all cells, approximately 85-90% were positive for Epcam staining. Of these cells, 5-15% were positive for Lgr5-eGFP. The percentage of Lgr5 high, medium and low population was 20%, 20% and 60% respectively in SI and 15%, 15% and 70% respectively in LI.
Gating strategy	Dead cells were eliminated by gating of forward/side scatter, forward/pulse-width parameters, and negative staining for 7-AAD (eBioScience). Lgr5+ cells were sorted by positive staining for Epcam (CD326) (BD Bioscience, Cat #563214) and endogenous Lgr5-GFP signal.

☒ Tick this box to confirm that a figure exemplifying the gating strategy is provided in the Supplementary Information.